ABSTRACT

Title of Document: PROCEDURES TO OBTAIN ACCURATE MEASUREMENT FROM A GAS FUELD BURNER

Hyeon Kim, Master of Science, 2014

Directed By: Associate Professor Peter B. Sunderland
Department of Fire Protection Engineering

Professor Emeritus James G. Quintiere
Department of Fire Protection Engineering

John de Ris
FM Global, Retired

Procedures to obtain accurate heat flux measurements from a 50 mm diameter gas-fueled burner using a diluent fuel gas mixture were examined that required following steps. Local heat flux measurements on the surface of a thick porous copper plate burner were corrected with a pure convective burning assumption and stagnant layer solution. Calibration procedures for thermopile-type heat flux gauge was developed and compared with NIST BFRL heat flux gauge calibration system. Calibration of gauges has found to be possible without controlling the temperature. The absorptivity and emissivity of the coating used on the burner and heat flux gauges were measured via calibrated heat flux gauges and copper slug calorimeter. Independently, an apparatus was designed, built, and calibrated to measure burner flame radiant fraction. The heat flux distribution at the burner was measured. Sample measurements were taken to show accurate measurements and potential analysis of the collected burner data is examined.

PROCEDURES TO OBTAIN ACCURATE MEASUREMENT FROM A GAS FUELD BURNER

By

Hyeon Kim

Thesis submitted to the Faculty of the Graduate School of the
University of Maryland, College Park, in partial fulfillment
of the requirements for the degree of
Master of Science
2014

Advisory Committee:
Associate Professor Peter B. Sunderland, Chair
Professor Emeritus James G. Quintiere
Assistant Professor Michael J. Gollner

Acknowledgements

I would have never been able to finish without the guidance of my advisors, help from my friends, and support from my family.

Foremost, I would like to express my sincere gratitude to my advisors for the excellent guidance and patience. Dr. Quintiere, Dr. Sunderland, and Dr. deRis has provided me a great atmosphere for research and learning. They have provided me with invaluable advice and support throughout my research. It is only due to their kindness, encouragement and patience that I have finished my thesis.

I would like to thank all the people in the fire protection engineering department. I was very fortunate to have learned under very knowledgeable professors whom I could always visit for advice. Also, my fellow graduate students for their support and friendship. I am very thankful for administrative support from Mary Lou, Sharon and Nicole. Without their support, I would likely not have graduated on time.

I would like to thank my parents and my friends. They were always supporting me and encouraging me with their best wishes. Finally, I would like to thank my significant other, Brittany Mills, for always being there cheering me up and standing by me.

Table of Contents

List of Tables

List of Figures

List of Symbols

B	Spalding B number; $B \equiv \frac{\frac{Y_{ox,\infty}\Delta h_c}{r} - c_p(T_H - T_\infty)}{L}$
C	Calibration constant
c_p	Specific heat capacity
D	Diameter
E	Voltage
F	View Factor
Gr	Grashof number
h	Convective heat transfer coefficient
ΔH_c	Effective heat of combustion
$\Delta H_{c,theory}$	Theoretical heat of combustion
h_{vap}	Heat of vaporization
k	Thermal conductivity
L	Heat of gasification
$\dot{m}$"	Mass flux
$\dot{M}$	Mass flow
Nu	Nusselt number
Pr	Prandtl number
$\dot{q_r''}$	Incident heat flux
R	Radious
T	Temperature
T_g	Gauge temperature
ΔT	Temperature difference
V	Voltage
$Y_{ox,\infty}$	Oxygen mass fraction
Δx	Distance difference
X_r	Flame radiant fraction
α	Absorptance of the heat flux gauge
α_T	Thermal diffusivity
ϵ	Emissivity of the heat flux gauge
ν	Kinematic viscosity
σ	Stefan-Boltzmann constant (5.670×10^{-11} kW/(m^{-2}·K^{-4}))

Subscripts

B	Blowing
f	Flame
g	Heat flux gauge surface
F	Fuel
s	Burner surface
∞	Ambient

Chapter 1: Introduction

1.1 Motivation and Objective

The goal of this study is to ensure accurate heat flux measurement from a gas fueled burner for emulation of condensed phase burning. Engineering approximations were made for past heat flux measurements on the burner surface. The current research provides procedures to obtain accurate heat flux measurements by correcting for fuel blowing effect caused by burner temperature rise during experiment. The correction process requires careful calibration of heat flux gauge and characterizing the absorptivity and emissivity of paint coating on the surface of the gauge and burner. The components needed for the correction process are examined. Independent of the burner and heat flux gauge, an apparatus designed to measure flame radiant fraction was built. With the help of past and current research, the BRE experiment is approved for future space flight mission to the International Space Station with NASA.

The adjustment of heat flux, mass flow rate of fuel/inert gas mixture, and burner surface temperature allows the emulation of the burning characteristics of condensed fuels. By burning fuel/inert gas mixture, the effective heats of gasification of the gas mixture can be matched to the heat of gasification of condensed fuels, hence the name Burning Rate Emulator (BRE). Previous work has been hindered with issues with ensuring correct heat flux measures are obtained from the gauges. The first iteration of the BRE was constructed with a brass body and thin brass screen burning surface which is embedded with thermopile type heat flux gauges. Previously, the sensors were supplied with 60°C water to prevent condensation of combustion products. Question on the accuracy of the

sensor measurement arose during experiment due to various correction factors. Further, the heat flux distribution to the surface was unknown and simple weighted average was used with two local measurements to approximate the average heat flux.

The second iteration of the BRE burner, the accuracy of heat flux measurements were sought after with characterization of the heat flux distribution into the burning surface. The newest BRE burner is constructed with a thick porous copper plate as a burning surface with embedded thermopile type heat flux gauges. Further development is being done to use the copper plate as a calorimeter to deduce the heat flux to the surface by heat transfer analysis. In the new burner, the heat flux gauges are not supplied with cooling water because of two reasons. First, water cooling will not be provided in the microgravity measurements. Second, the water cooling has a minor effect on the burner surface temperature.

All heat flux gauges used in the experiments were carefully calibrated against a standard heat flux gauge that traces back to NIST. The gauges were also shown to correctly measure the incident heat flux without cooling water. Measurement correction procedures were developed to account for interoperation of the gauge and burner surface temperature and blockage effect. The absorptivity and emissivity of the paint used in the burner surface and heat flux gauge surface that is needed in the analysis were found. Preliminary heat flux distribution into the burner surface is obtained through modifying the brass screen burner to embed gauges in multiple radial locations. Independent of the burner, a radiometer was built to measure the flame radiation fraction from the burner flame. Through these steps, accurate measurements of various components needed for analysis are obtained.

1.2 Literature review and background

Emulation of solid and liquid fuels using gaseous burner has been done previously. Orloff and deRis pioneered the use of sintered metal burner to study steady burning of condensed-phase fuel to model ceiling orientations [5]. In this study, a fuel-inert gas mixture was flowed through a sintered metal burner that allowed the B number to be varied. Kim et al. examined the vertical, inclined, and horizontal cylindrical fuel surfaces with different chemical parameters to estimate burning parameter of chemically complex fuel [6]. Large scale sintered metal burner were examined by deRis et al. to examine turbulent flames in various inclination [7]. These burners used water-cooled burner surface to obtain the flame heat flux. The result of these experiments by looking at mainly convective burning, showed that the B number controls the burning rate of condensed fuels. Further, it showed that emulation of solid and liquid fuel is possible through varying fuel-inert gas mixture composition to match the heat of gasification or B number. Porous burner was used in microgravity by Brahmi et al. [8], but flame heat flux was not measured and results were not analyzed in terms of condensed-phase properties.

Perfect emulation of condensed fuel using a burner cannot be done. The design of the burner used by deRis et al. and BRE burner maintains a uniform fuel velocity over the burning surface, which is untrue for real fuel. In burning of liquid fuels, the heat flux distribution into the burner surface creates different fuel mass flux over the surface. However, previous research [1-3] showed good agreement with laminar convective theory, which suggests that the fuel velocity on top of the burner face quickly equilibrates to proper diffusional flow.

The BRE study started with Zhang et al. by showing another validation of burning emulation by comparing the flame standoff distance in inclined plates [9]. Bustamante, showed BRE flame stand-off distance showed reasonable agreement when emulating methanol [10].

Validation experiments using the brass screen BRE was conducted through emulation of methanol, heptane, PMMA, and POM. The mass loss rate of real fuel of 50 mm diameter was measured and matched with the BRE. The heat of combustion was matched to obtain the flame height. The sooting tendencies of the emulated fuels were considered in which methane was used to emulate methanol and POM, ethylene for heptane and propene for PMMA. The validation results are shown in Table 1.1.

		$\dot{m}''$	Δh_c	SP	T_s	L
Methanol	Pool	11	19	∞	64	1.2
	BRE (X_{CH4} = 52%, X_{N2} = 48%)	11	19	∞	160	1.24
Heptane	Pool	15	41.2	139	98	0.48
	BRE (C2H4)	15	41.5	120	211	0.51
PMMA	Pool	6	24.2	105	390	1.6
	BRE (X_{C3H6} = 50%, X_{N2} = 50%)	6	24.3	117	312	1.8
POM	Pool	9	14.4	∞	420	2.4
	BRE (X_{CH4} = 41%, X_{N2} = 59%)	9	14.1	∞	167	2.1

Table 1.1 Burning rate emulation using brass screen BRE burner

The flame size, shape, and color of the emulated flame closely resembles to that of the real fuels, Figure 1.1.

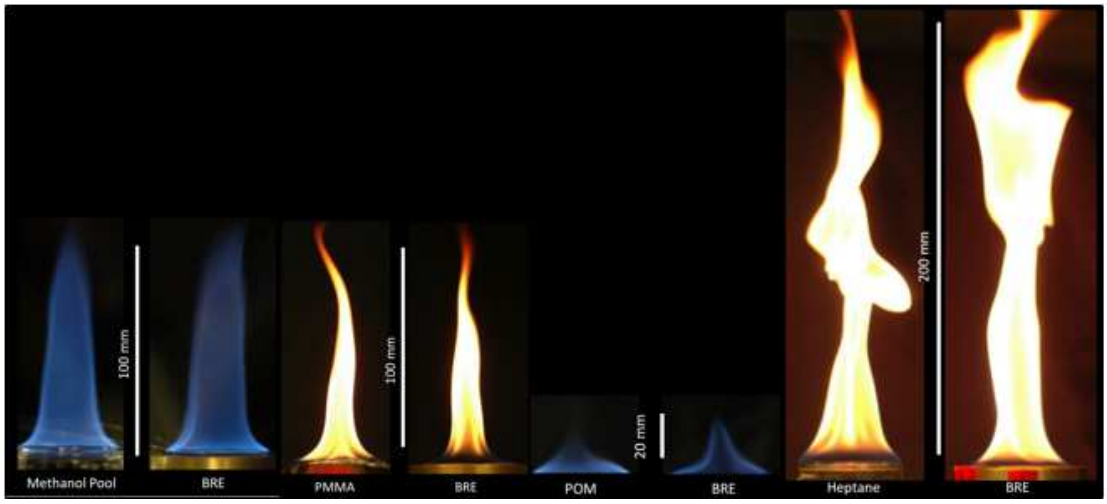

Figure 1.1 Comparison of burning of emulated BRE flame and real fuel

The ongoing experiments with the copper plate burner will produce more accurate heat flux measurements which will allow better emulation.

Chapter 2: Burning Rate Emulator Burner Design and Heat Flux Gauge Measurement Correction

The BRE theory is examined. By matching the heat of combustion, heat of gasification, smoke point, flow rate of the gas mixture, and the burner surface temperature using fuel and dilution mixture allow the emulation of burning characteristics of condensed fuels, hence the name "Burning Rate Emulator". Currently, two different iteration of the BRE burner have been designed and are being used in experiments. The original BRE burner has a porous burning surface made of thin brass screen and the new BRE burner has a surface made of a thick porous copper plate.

The heat flux gauge and the burner surface temperature is not controlled. Two measurement correction procedures were considered and its correction magnitude examined.

2.1 BRE design and construction

The original BRE is constructed of entirely in brass held together with silver solder. Two Medtherm thermopile type 1/8th inch diameter water cooled heat flux sensors are located at the center (0 mm) and at edge (15 mm). Two thermocouples are tied into the brass screen to measure the burning surface temperature. The burner plenum is maximized and filled with glass beads to encourage mixing of the incoming fuel stream from beneath the base. The two heat flux gauges only gives the local measurements, but not the average heat flux to the entire burner surface that is needed in the analysis. Originally, a weighted average of $0.36 * \dot{q}^{"}_{center} + 0.64 * \dot{q}^{"}_{edge}$ was used with the two

heat flux gauges to obtain the average heat flux without estimating the entire distribution. Figure 2.1 shows the brass screen BRE.

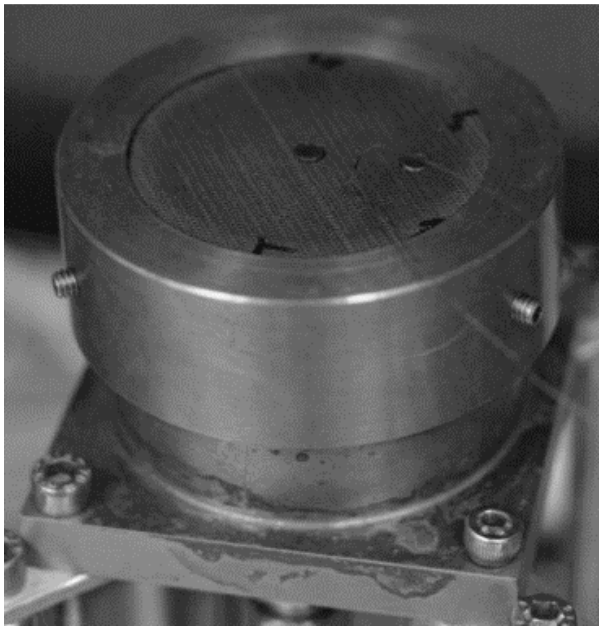

Figure 2.1 Brass screen original BRE burner

A new BRE burner was designed and constructed with the goal to obtain a better heat flux measurement and distribution on the burner surface. The new burner design uses a thick porous copper plate instead of a thin brass screen. The thick porous copper plate is used as a calorimeter and a heat transfer analysis is used to deduce the average heat flux to the burner surface. A stainless steel body and base plate were specified to minimize heat transfer from the copper plate to the burner body. Like the old burner, two Medtherm thermopile type $1/8^{th}$ inch heat flux gauges are used at the center and edge; 16 mm away from the center. The heat flux gauges have the capability of being water cooled, but temperatures were not controlled for the experiment to keep the measurement consistent with microgravity drop tower experiments where water cooling cannot be incorporated. Instead, the heat flux gauges are corrected for

temperature rise using gauge and burner surface temperatures with pure convective burning assumption and pure convention stagnant layer solution. The thick porous copper plate burner is shown in Figure 2.2.

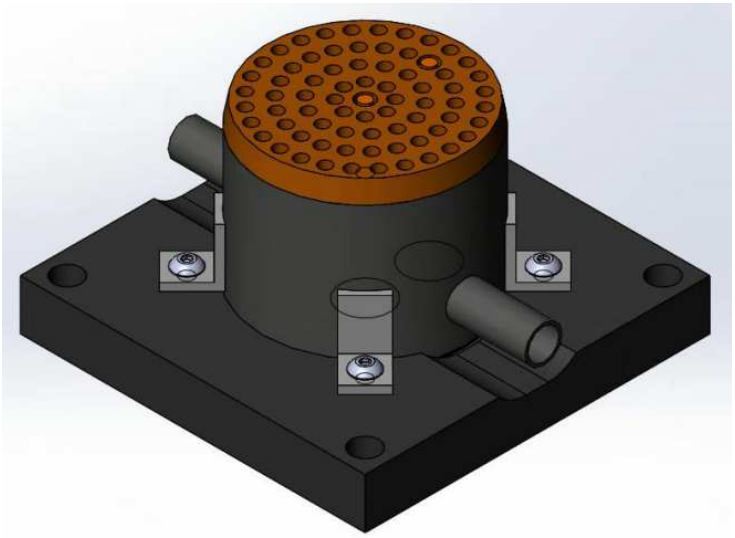

Figure 2.2 Porous copper plate BRE burner

Two thermocouples are attached to the top of the burner surface via small pre drilled holes. A third thermocouple is attached at the burner body. The plenum inside the burner have been specially designed to minimize heat transfer into the body from the copper plate. The gas flow uniformity is achieved using a ceramic honeycomb material. Fuel mixture is ensured by dividing the incoming gas flow into two opposing sides of the burner, Figure 2.3.

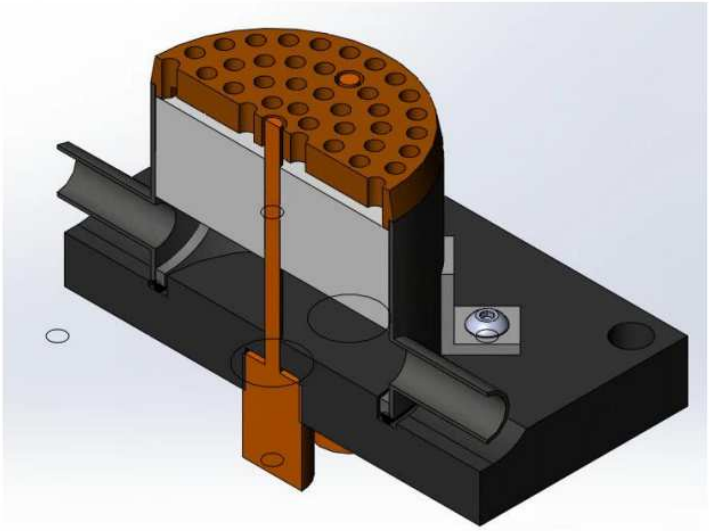

Figure 2.3 Porous copper plate BRE burner section view

Leakage of the gas mixture is prevented through of use of rubber O-rings between the burner body and heat flux gauges and contact with the burner base plate. The copper burner surface and the heat flux gauges are painted with flat black Rust-Oleum High Heat paint which the absorptivity and emissivity was found using experiments. This paint has been carefully selected to be able to withstand high degree of thermal degradation with minimal gas emission during experiments. The burner is wrapped with 1/8th inch thick Cotronic Corp. 3000°F Ceramic Paper for insulation to minimize convective heat transfer losses from the burner housing. Figure 2.4 shows the completed burner.

Figure 2.4. Completed porous copper plate BRE burner

A smaller 25 mm version of the thick porous copper plate burner is constructed for 5 second Drop Tower testing at NASA Glenn Research Center. Unlike the 50 mm version, two thermocouples are set in place on the underside of the copper plate via small pre drilled holes and high temperature epoxy.

2.2 BRE design theory

The basis of BRE design stems from the theory of steady burning for an evaporating condensed fuel. A comparison is made to an infinitely thick pool fire case with steady burning, Figure 2.5.

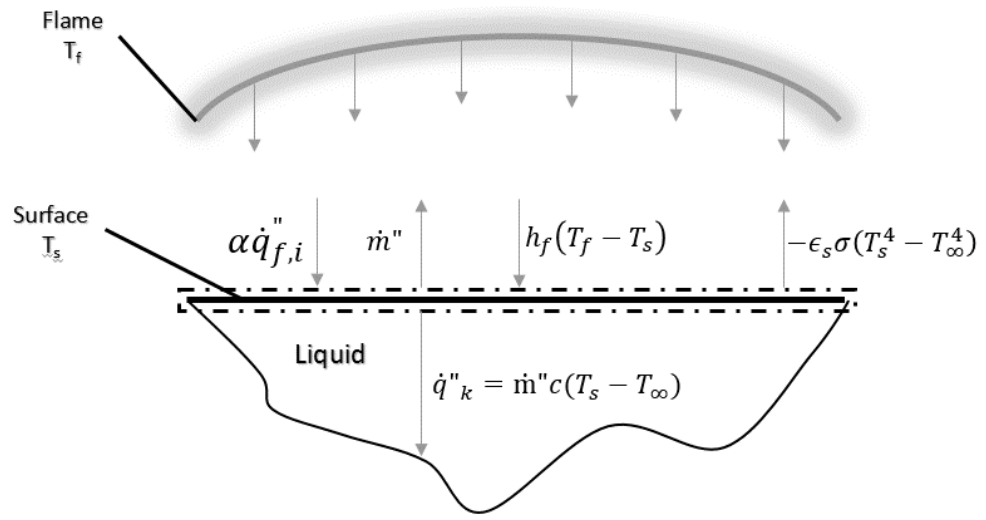

Figure 2.5 Liquid steady burning case

Heat balance on the burning surface yields,

$$\dot{m}''h_{fg} = \alpha\dot{q}''_f - \epsilon_s\sigma(T_s^4 - T_\infty^4) + h_f(T_f - T_s) - \dot{m}''c(T_s - T_\infty) \tag{2.1}$$

Where the radiation, re-radiation, and convection terms describe the net heat flux to the surface with the last term describing conduction into the infinitely thick liquid,

$$\dot{q}''_k = \dot{m}''c(T_s - T_\infty) \tag{2.2}$$

The net heat flux to the surface is,

$$\dot{q}''_{net\ surface} = \alpha\dot{q}''_f - \epsilon_s\sigma(T_s^4 - T_\infty^4) + h_f(T_f - T_s) \tag{2.3}$$

Reorganization of the surface heat balance yields,

$$\dot{q}''_{net\ surface} = \dot{m}''[h_{fg} + c(T_s - T_\infty)] \tag{2.4}$$

Where,

$$L = h_{fg} + c(T_s - T_\infty) \tag{2.5}$$

Thus, steady burning can be put in terms of heat of gasification, L.

$$\dot{m}'' = \frac{\dot{q}''_{net\ surface}}{L} \tag{2.6}$$

The steady burning of infinitely deep liquid can be transposed to a steady burning on top of a burner to find an analogous heat of gasification, L, which is related to the net incident heat flux into the surface. The burner has two heat flux gauges that are positioned flushed to the burner surface to measure the local heat flux from the flame, Figure 2.6.

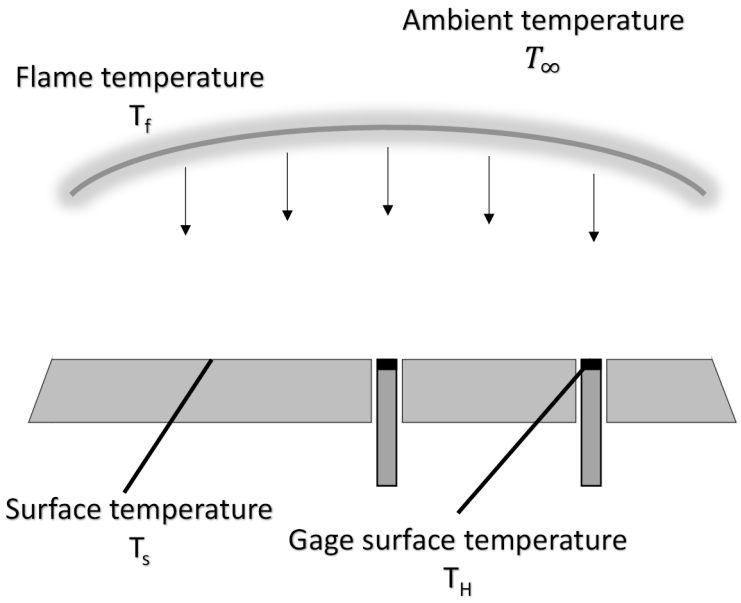

Figure 2.6. Burner steady burning

Similar to the infinitely thick liquid scenario, the net heat flux is composed of the absorbed flame radiation, the flame convection to the surface, and the re-radiation heat loss. The burner and gauge surface temperatures are not controlled, as a result the two temperatures always differ during burner operation. Careful consideration burner surface and heat flux gauge must be taken in order to carefully correct for the temperature differences.

The local steady mass flux at a point is expressed for a given surface temperature and flame temperature.

$$\dot{m}^{"} L = \dot{q}^{"}_{net} = \alpha_s \dot{q}^{"}_r - \epsilon_s \sigma (T_s^4 - T_\infty^4) + h_B \left(T_f - T_s\right) \tag{2.7}$$

Where $h_B$convective heat transfer coefficient with blowing effect that is caused by transverse flow of fuel vapor. Compared to natural convection coefficient, h_B is slightly lower because of the increased boundary layer of fuel flow that makes the overall heat transfer to the burners more difficult.

The absorbed heat flux into the heat flux gauge is expressed in terms of the voltage output and the calibration constant,

$$CE = \alpha_H \dot{q}^{"}_r - \epsilon_H \sigma (T_H^4 - T_\infty^4) + h_B \left(T_f - T_s\right) \tag{2.8}$$

Subtracting the two equations yields,

$$\begin{aligned} \dot{m} L = CE + (\alpha_s - \alpha_H) \dot{q}^{"}_r - \epsilon_s \sigma (T_s^4 - T_\infty^4) + \epsilon_H \sigma (T_H^4 - T_\infty^4) \\ + h_B (T_H - T_s) \end{aligned} \tag{2.9}$$

Same absorptivity and emissivity is achieved in both the burner and gauge surfaces by using same paint with known value of emissivity and absorptivity. Finally, an equivalent theory of steady burning is derived for the burner.

$$\dot{m}^{"} = \frac{CE + \epsilon \sigma (T_H^4 - T_s^4) + h_B (T_H - T_s)}{L} \tag{2.10}$$

The net heat flux is found using the sensor voltage and calibration constant with correction factor that includes the surface absorptivity and emissivity, burner and gauge surface temperature, and the convective heat transfer coefficient with blowing.

$$Correction = \epsilon \sigma (T_H^4 - T_s^4) + h_B (T_H - T_s) \tag{2.11}$$

The correction due to blowing effect must be estimated. This was done using two different approaches.

2.3 Estimation of convective heat transfer coefficient with blowing using heat transfer correlation

Using heat transfer correlation gives one method for estimating h_B. The convective coefficient with blowing effect is described by,

$$h_B = h\frac{\ln(1+B)}{B} \tag{2.12}$$

Where ln(1+B)/B is blocking factor that enlarge the boundary layer due to blowing effects [11]. The pure convection stagnant layer solution gives,

$$\dot{m}'' = \frac{h}{c_p}\ln(1+B) \tag{2.13}$$

Set λ

$$\lambda = \frac{c_p \dot{m}''}{h} = \ln(1+B) \tag{2.14}$$

Combining the convective coefficient with blowing effect with the stagnant layer solution results in,

$$h_B = h\left(\frac{\lambda}{e^{\lambda}-1}\right) \tag{2.15}$$

Then, the convective heat transfer coefficient is estimated using pure heat transfer correlation. Approximate solution to natural convection from a horizontal cylinder is used for the burner surface [12],

$$h = 1.32\left(\frac{T_s - T_\infty}{D}\right)^{\frac{1}{4}} \tag{2.16}$$

The convective coefficient must be approximated to obtain coefficient with blowing effect. However, for microgravity experiments, the convective coefficient is unknown and a different approach must be used to approximate the blowing effect.

2.4 Estimation of convective heat transfer coefficient with blowing using pure convective burning assumption

Pure convective burning assumption give a second way of approximating h_B. This approach can used without estimating the convective coefficient. The convective coefficient with blowing effect is described by,

$$h_B = h\frac{\ln(1+B)}{B} \tag{2.17}$$

The pure convection stagnant layer solution gives,

$$\dot{m}'' = \frac{h}{c_p}\ln(1+B) \tag{2.18}$$

Spalding B number is defined as [11],

$$B = \frac{\frac{Y_{ox,\infty}\Delta h_c}{r} - c_p(T_H - T_\infty)}{L} \tag{2.19}$$

Combining the three equations gets the mass flux,

$$\dot{m}'' = \frac{h_B}{c_p}\left(\frac{\frac{Y_{ox,\infty}\Delta h_c}{r} - c_p(T_H - T_\infty)}{L}\right) \tag{2.20}$$

Which can be shown with flame heat flux,

$$\dot{q}_f'' = \dot{m}''L = h_B\left[\frac{Y_{ox,\infty}\Delta h_c}{c_p r} - (T_H - T_\infty)\right] \tag{2.21}$$

Thus, the convective heat flux with blowing effect is found,

$$h_B = \frac{\dot{q}_f^{"}}{\frac{Y_{ox,\infty}\Delta h_c}{c_p r} - (T_H - T_\infty)} \tag{2.22}$$

The heat flux gauge measurement gives,

$$\dot{q}_f^{"} = CE - \epsilon\sigma(T_H^4 - T_\infty^4) \tag{2.23}$$

This approximation using pre convection burning assumption is preferred because it can be used in both 0G and 1G gravity experiments. But the approximation can only give local mass flux at a point source. Further work is being done to obtain the overall averaged heat flux distribution on the burner surface by using the thick copper plate as a calorimeter.

2.5 Heat flux correction calculations and magnitude of correction

The magnitude of correction differs between the two heat flux measurements because it uses different assumptions. The procedures used to correct for this effect is detailed in this section. An example case of methanol emulation is examined with methane flow rate of 13.39 mg/s and nitrogen flow of 8.21 mg/s with a total burning rate of 11 g/m^{2}s. Figure 2.8 and 2.9 shows raw data for this emulation. Two thermocouples are attached at the burner surface to measure its temperature. A third thermocouple is attached to the body to measure the overall burner temperature. Two 1/8th inch heat flux gauge is positioned flushed to the burner surface and each gauge is equipped with a Type-T thermocouple to measure the surface temperature.

Ten minutes of methanol emulation data were collected to allow sufficient time for the burner surface to rise in temperature. Figure 2.7 shows the voltage measurements by

the heat flux gauges and Figure 2.8 shows the average surface temperature and the heat flux gauge surface temperature.

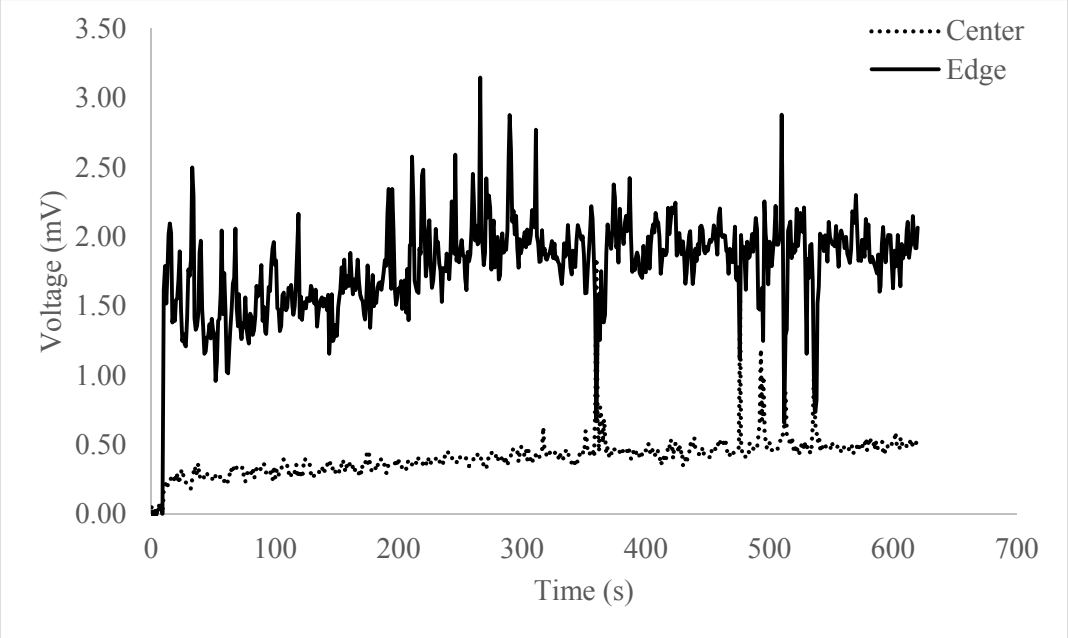

Figure 2.7 Voltage measurement using two heat flux gauges.

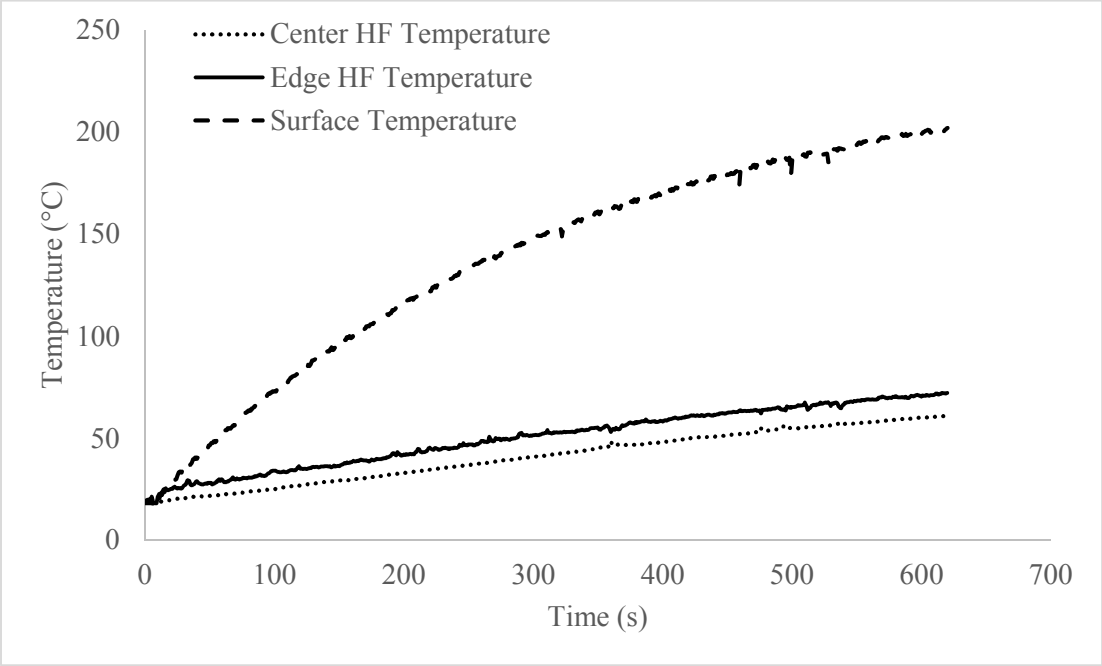

Figure 2.8 BRE burner surface and heat flux gauge surface temperature

The heat transfer correlation method of estimating h_B is examined first. The heat transfer correlation method approximates the convective coefficient of the overall burner surface. Equation 2.15 is used to find the convective heat transfer coefficient of the burner surface. Equation 2.14 is then used to modify the results to correct for blowing effect. Both the convective coefficient and modified coefficient with blowing is shown below.

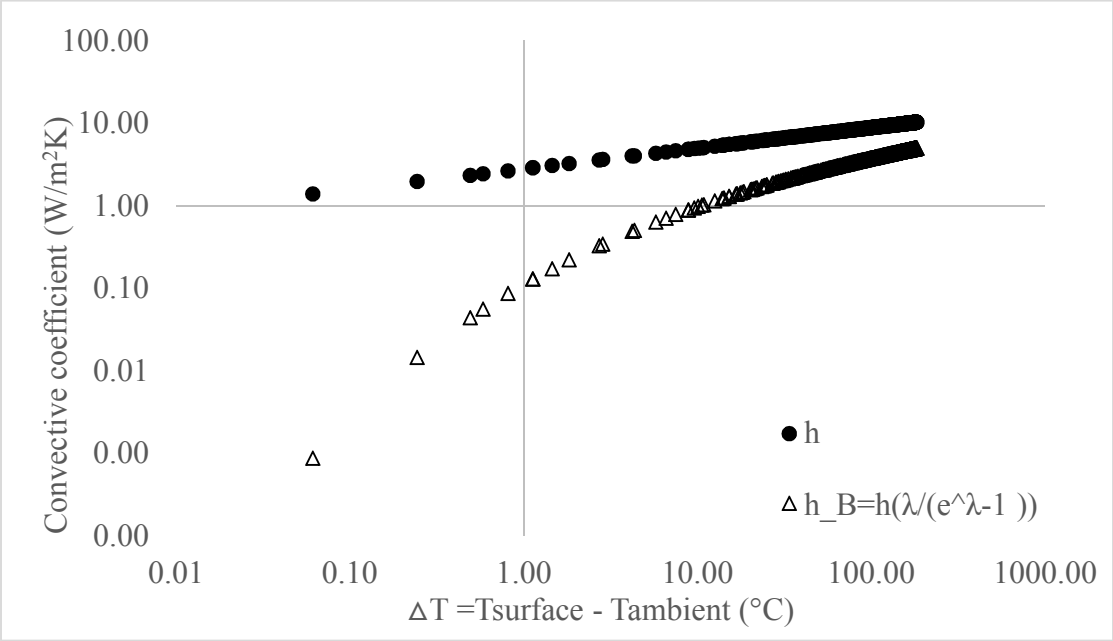

Figure 2.9 Calculated convective coefficient versus ΔT in log-log plot

The estimation of h_B using the pure convective burning assumption is examined. Equations 2.20 and 2.21 are used in conjunction to estimate local values of h_B at two different heat flux gauge location. The results are compared with the heat transfer correlation method as shown in Figure 2.10.

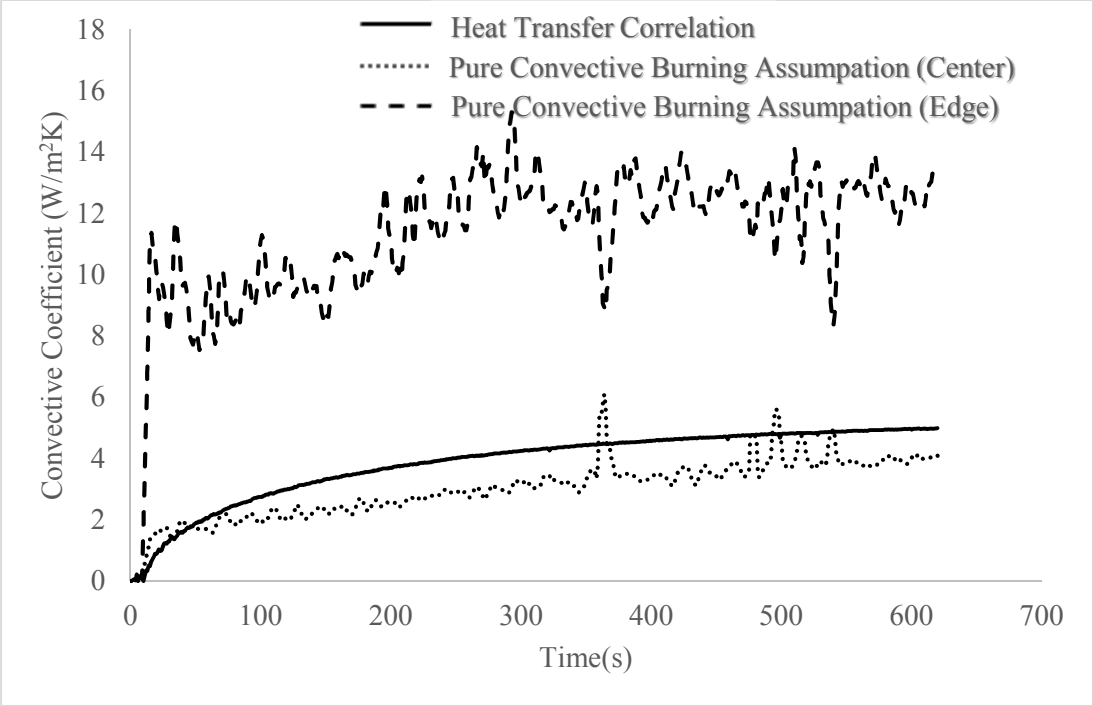

Figure 2.10 Calculated convective coefficient suing pure convective burning assumption

Using the estimated h_B, the total correction term and Equation 2.11, the result is calculated and plotted in Figure 2.11 and Figure 2.12 for the two different methods. The total magnitude of the correction differs by ~1 kW/m^{2}s for edge heat flux measurement and ~0.2 kW/m^{2}s for center heat flux measurement.

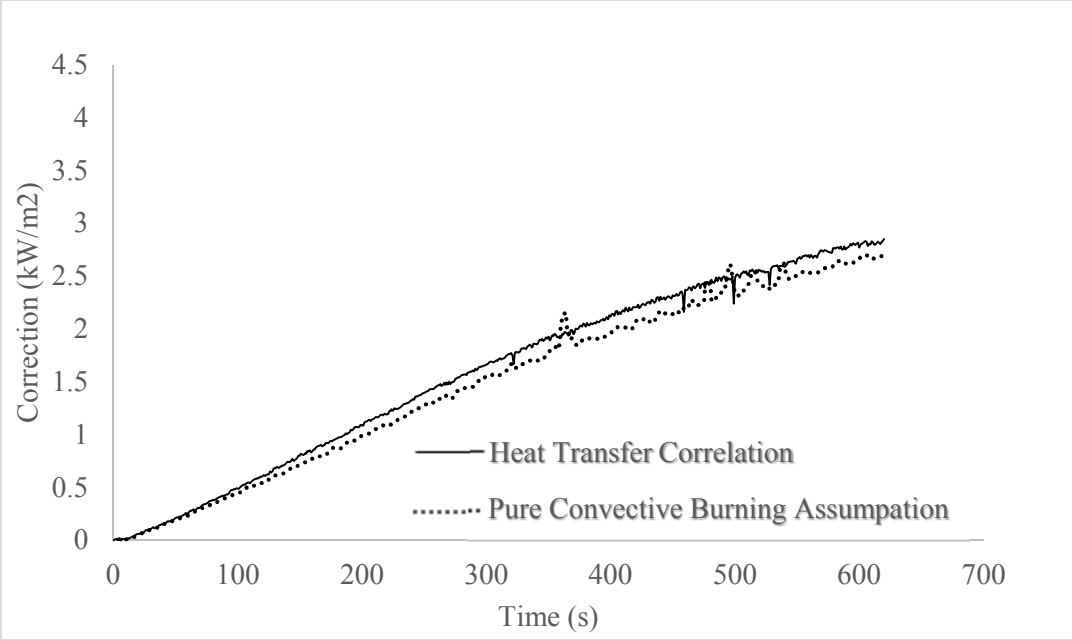

Figure 2.11 Calculated correction for center heat flux gauge

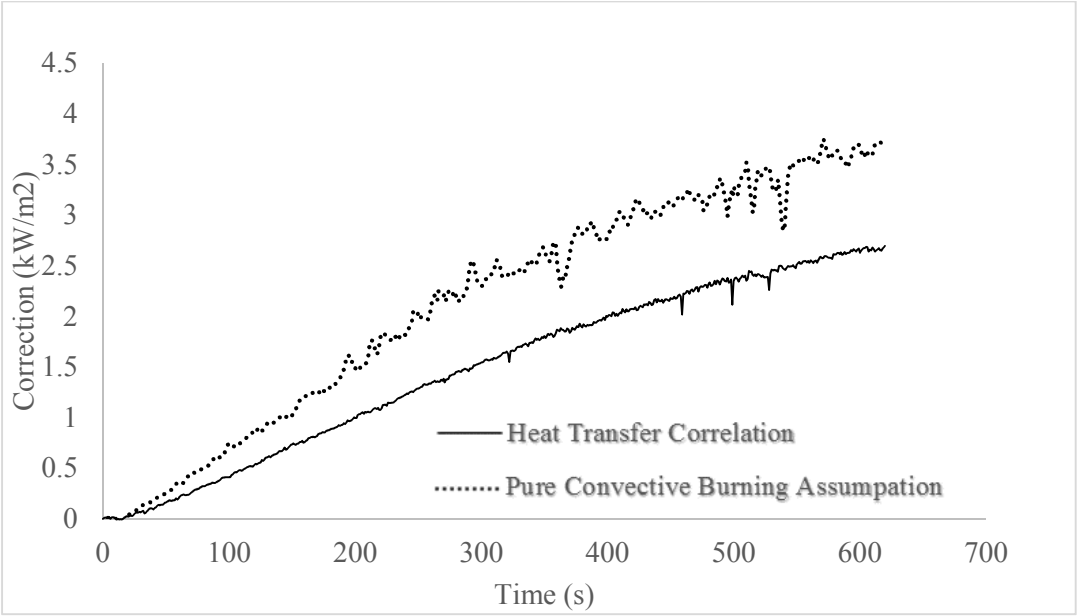

Figure 2.12 Calculated correction for edge heat flux gauge

The differences between the two methods are small and both could be used to correct for temperature and blowing effect to calculate the heat flux measurement. However, the second method using the pure convective burning assumption is preferred to be

used so that the analysis is consistent with microgravity measurements. The heat transfer correlation method can be used but the convective heat transfer coefficient on the surface of the burner is difficult to estimate under microgravity, but can be found experimentally.

Chapter 3: Calibration of Heat Flux Gauges

The steady burning analysis of BRE flames is critically dependent of the heat flux measurements using the two embedded heat flux gauges. Calibration and use of the heat flux gauges must be carefully considered to ensure correct values are measured. All gauges used in the BRE experiments traced back to NIST's heat flux gauge calibration system. Calibration in UMD laboratory with radiant panel is examined. Further, it is shown that the gauges can correctly be calibrated and measure the incident heat flux without the use of cooling water.

3.1 Calibration of Heat Flux Gauges

The Schimidt-Boelter gauges are often used in fire testing to measure the incident heat flux given from a flame as well as within the burner. The calibration of the heat flux gauge in UMD is done by mounting the gauge so that the surface is perpendicular to the radiant panal and cooled by circulating water to minimize the effect of convective and radiative loss at the surface. The heat flux is measured by using a voltage output generated from heat conduction through a thermopile, Figure 3.1.

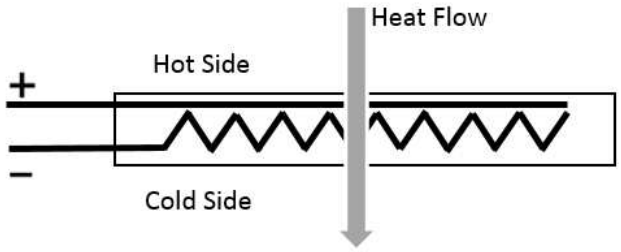

Figure 3.1. Thermopile construction on heat flux gages.

The heat flux is absorbed at the surface and is transferred to a heat sink that remains at a different temperature than the surface. The temperature difference between the

surface and the heat sink is a function of the heat transfer and the net absorbed heat flux. Between the two points, the thermopile forms a differential thermoelectric circuit that generates a voltage directly proportional to the heat transfer rate. The voltage reading then is directly related to a constant to obtain the incident heat flux.

The gauge's voltage output is directly proportional to the net absorbed heat flux, directly converting voltage reading to heat flux will give a different value than the actual incident flame heat flux. Gains and/or losses through convection and radiation will affect the voltage output of the gage. It is possible to correct the difference by including convection and radiation correction term when calculating the incident heat flux from the voltage reading.

The response time of the gauge differs depending on the incident radiant heat input. For Medtherm 64 series Gardon or Schimidt-Boelter gauges, the response time is listed as follows [13].

250 to 4000 BTU/(ft^2-s): less than 50 ms

50 to 200 BTU/(ft^2-s): less than 100 ms

2 to 30 BTU/(ft^2-s): less than 250 ms

3.2 Sensor response to ambient heat flux

The heat flux gauges respond to heat flux from both radiative and convective sources. The different flux can be distinguished by applying an energy balance to the gauge surface. The absorbed conductive heat flux through the sensor element is given by the calibration constant, C, of the particular sensor.

$$k\frac{\Delta T}{\Delta x} = C\mathrm{E} \tag{3.1}$$

This can be equated to the net surface heat flux for external radiative source,

$$\mathrm{CE} = \alpha q_r^{i\prime\prime} - h\left(T_g - T_\infty\right) - \varepsilon\sigma(T_g^4 - T_\infty^4) \tag{3.2}$$

The energy balance assumes a protruding sensor facing a purely radiative heat source. The losses at the surface is due to convection and re-radiation. Part of the radiation is absorbed and conducted through the sensor element. The degree of absorption is particular to a given coating and a given source. For radiative source, the two losses comes from convection and re-radiation. For convection, the heat transfer coefficient, h, will depend on the heat flux gauge's shape and orientation as well as the ambient flow conditions. The coefficient can be estimated or measured directly.

Sometimes, the manufacturer will give C in terms of the incident radiative heat flux,

$$C_{incident} = \frac{C_{absorbed}}{\alpha} \tag{3.3}$$

The $C_{incident}$ is effected by the surface absorptivity and the source radiation. Defining the calibration constant in terms of incident heat flux creates a particular concern as the measurement is particular to a given coating and a given source. Thus, depending on the radiation source, the calibration constant will differ from the manufacturer's value. Clear definition of the gauge coating and the source radiation is key to measuring what is absorbed on the surface then conducted through the sensor element. It is important to give some thought on types of surface coating and the source spectrum. In general, the emissivity of the coating depends on the thickness. The values quoted for coating are for infinite thickness what it is considered optically thick. However, when too thick, it will lower the sensor's response time.

Typically, gray body assumption is used to simplify the coating's emissivity and absorptivity by assuming no dependence of the source wavelength and treating as a constant value. However, the emissivity and absorptivity is dependent on the source spectrum. For example, a particular coating may have a very high reflectance from solar radiation, but very low for low temperature source radiation. The observed reflectance of the surface coating will change depending on the dominant spectrum of the source radiation. All coating exhibit this behavior to a certain degree.

3.3 Sensor calibration

In calibration of the heat flux gauge, the types of source radiation can range from a porous burner, tungsten lamp, blackbody, hot surfaces and etc. If using a blackbody as a source, Wein's displacement law can be used to determine the peak spectrum radiation. The wavelength can be compared to the surface coating's response to better approximate the surface reflectance. However, for radiation source such as porous burner, characterizing the spectrum will be difficult. Nevertheless, the behavior of the surface coating to the source should be thought through.

Prior to experiments with the BRE burner, there was a need to replace the UMD's laboratory standard. A new standard was established using the NIST's BFRL heat flux gauge calibration system [14]. 1 inch diameter Medtherm heat flux gauge, SN 180253, was used to establish a new laboratory standard by calibration against NIST's 1 inch diameter SN 124421 standard gage that was originally calibrated by the Radiometric Physics Division of the National Bureau of Standards (now NIST). The calibration system's heat source consists of a 2000 W tungsten halogen filament lamp. The amperage of the lamp is varied to achieve different heat fluxes of 2 to 15 kW/m^2.The

lamp is placed at one of the foci of a large ellipsoidal reflector, with the entrance to a kaleidoscope flux redistributor being locating at the other end. A metal housing surrounds the half of the ellipsoidal mirror containing the lamp [14].

The NIST calibration procedure for heat flux gage calibration using tungsten lamp is as follows:

1) Power on tungsten lamp at 2 kW/m^2 and let the lamp equilibrate for 20 minutes.
2) Adjust cooling flow at 0.2 gal/min at 20°C for both standard and un-calibrated gage.
3) Obtain a 60 second average using the standard gage.
4) Replace standard gage with un-calibrated gage and obtain 60 second average.
5) Replace with standard gage and obtain 60 second average to check for drift.

All of the heat flux gauges used with the BRE burner traces back to NIST's calibration system.

The calibration within the UMD was made by stripping the Medtherm paint of the un-calibrated gauges and repainted with 3M Nextel Suede Coating 3101 S 139 dark black using an airbrush. The sensor is repainted to match the paint on top of the BRE burner surface. An apparatus shown in Figure 3.2 is used to secure two gages at a time. The gages are held horizontally to one another and the holder can rotate to allow the gage to switch position. Radiant heat is provided by Dyna-Glo Tank Top Heater attached to a propane cylinder. The heat flux is varied by changing the distance between the gage and the heater.

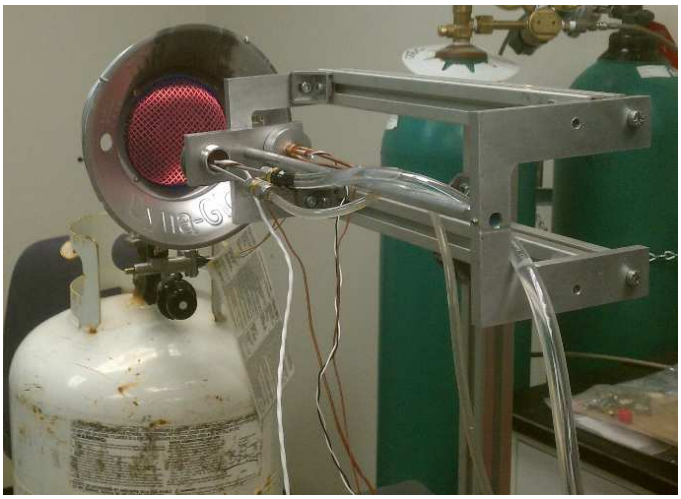

Figure 3.2 Heat flux gauge holder and radiant heater

In calibration using a radiative source, the ambient temperature must equal the gage temperature to negate or minimize errors through convective and re-radiative effects. With equal temperature, the equation # turns into.

$$CE = \alpha \dot{q}_r^{"} \tag{3.3}$$

A very simple way to ensure ambient temperature water is to have a water reservoir that is open to the laboratory air for a sufficiently long time for the water to equilibrate with the ambient temperature and circulate to the heat flux gauge using a water pump. An example of calibration using ambient temperature water is shown below in Table 3.1.

Measured Heat Flux 253 HF (kW/m^2)	Calibrated Gauge SN 180251 Voltage (V)	251 Absorbed Constant ($kW/m^2/mV$)
10.67	6.68E-04	15.65
10.17	6.56E-04	15.20
8.15	5.10E-04	15.67
7.90	5.02E-04	15.42
6.37	4.06E-04	15.36
6.31	3.92E-04	15.75

Table 3.1 Calibration data for $1/8^{th}$ inch SB heat flux gage.

The absorbed calibration constant used in experiments for all calibrated gauges are listed in the table below.

Serial Number	Absorbed kW/m^2 per mV
180251 (1/8th inch gauge)	15.51
180252 (1/8th inch gauge)	15.35
183743 (1/32th inch gauge)	16.00
183744 (1/32th inch gauge)	19.20
180253 (1 inch Laboratory Standard)	14.52
180254 (1 inch Transfer Standard)	11.77

Table 3.2 Absorbed calibration constant for six gauges used in the BRE project

3.4 Sensor calibration at varying temperatures

Sometimes, the gauges may need to be calibrated and operated at various temperatures away from the ambient temperatures. In this case, the 1/8th Medtherm heat flux gauge used in the BRE burner is not water cooled and is free to rise in temperature. The higher temperature at the surface of the gauge causes convective and radiative losses that decreases the sensor element's voltage output.

$$Losses = -h(T_g - T_\infty) - \varepsilon\sigma(T_g^4 - T_\infty^4) \quad (3.4)$$

To correct for the losses, the gauge's convective heat transfer coefficient needs to be determined. The convective heat transfer coefficient increases with temperature, scaling with $\Delta T^{1/4}$ in a quiescent ambient environment. The gauge temperature and ambient temperature is needed as well as the absorbed heat flux measurement. If the incident heat flux is known, a convective coefficient can be calculated for the specific gage temperature to the ambient temperature.

$$h = \frac{\alpha \dot{q_r}'' - CE - \varepsilon\sigma\left(T_g^4 - T_\infty^4\right)}{T_g - T_\infty} \tag{3.5}$$

The actual heat flux is measured using a water cooled gauge and the heat flux gauge in question is supplied with heated water between 40°C to 75°C. The convective heat transfer coefficient is then calculated using equation 3.5. The result of calculated h is shown in Figure 3.3.

Alternatively, an engineering estimation of the convective coefficient can be made using heat transfer correlations starting with the Nusselt number correlation,

$$h = \frac{Nu * k}{L} \tag{3.6}$$

The Nusselt number correlation for national convection with vertical flat plates for Ra $\leq 10^9$,

$$Nu = 0.68 + \frac{\left(0.670\ (Gr * \mathrm{Pr})^{\frac{1}{4}}\right)}{\left(1 + \left(\frac{0.492}{Pr}\right)^{\frac{9}{16}}\right)^{\frac{8}{27}}} \tag{3.7}$$

Grashof number for vertical flat plates,

$$Gr = \frac{g\left(\frac{1}{\overline{T}}\right)\left(T_g - T_\infty\right)L^3}{\nu^2} \tag{3.8}$$

And Prandtl number,

$$\mathrm{Pr} = \frac{\nu}{\alpha_T} \tag{3.9}$$

The heat transfer correlation method underestimates the convective heat transfer coefficient compared to the measurement method, Figure 3.3. Nevertheless, it will give

an approximate value that can be applied to correct for the convective losses at the surface.

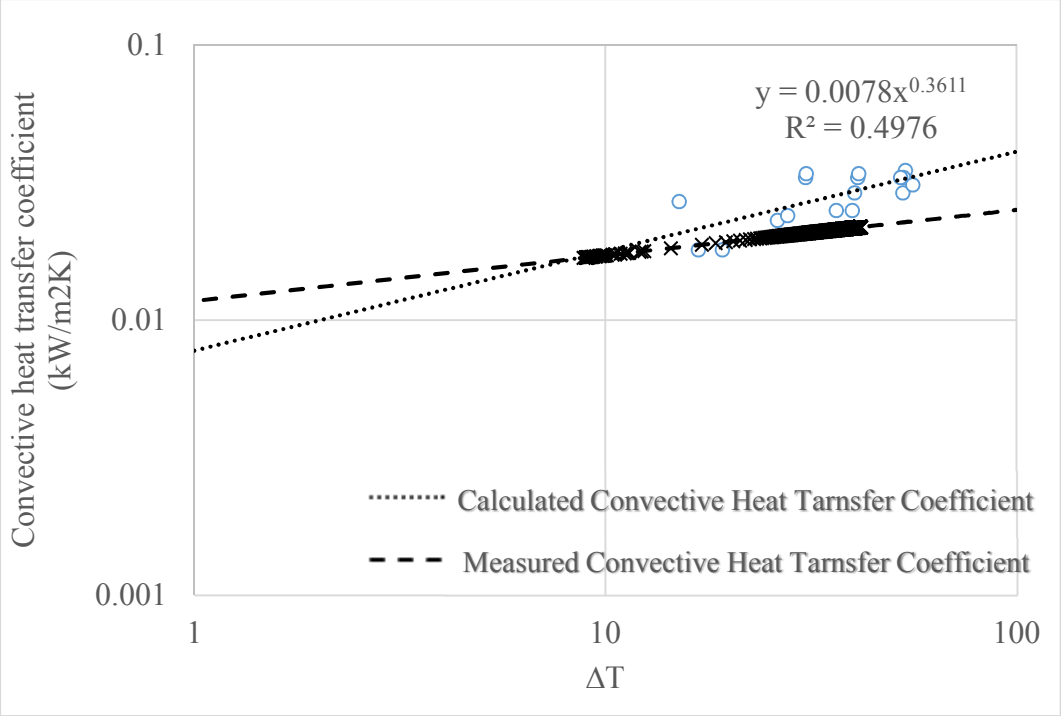

Figure 3.3 Measured and calculated convective heat transfer coefficient

The convective heat transfer coefficient measurement is very difficult. The measurement responded to the slightest variance within the surrounding area and by any unforeseen drafts cause by opening doors and activation of various fume hoods within the laboratory. The heat transfer coefficient, in theory, should scale with the $\Delta T^{1/4}$ relationship. The curve fit scale to 0.38. With more measurement with more water temperature variance, better relationship could be found.

The measure convective heat transfer coefficient can then be applied to actual measurements to correct for the voltage loss by applying the result,

$$h = 0.0078(\Delta T)^{0.3611} \tag{3.10}$$

Heat flux measurement uncorrected for temperature rise using a 1/8th inch Medtherm gauge is shown in Figure 3.4. The measurements are compared with the actual heat flux, 38 kW/m^2. Figure 3.5 shows the corrected heat flux measurement using the measured convective heat transfer coefficient, Equation 3.10.

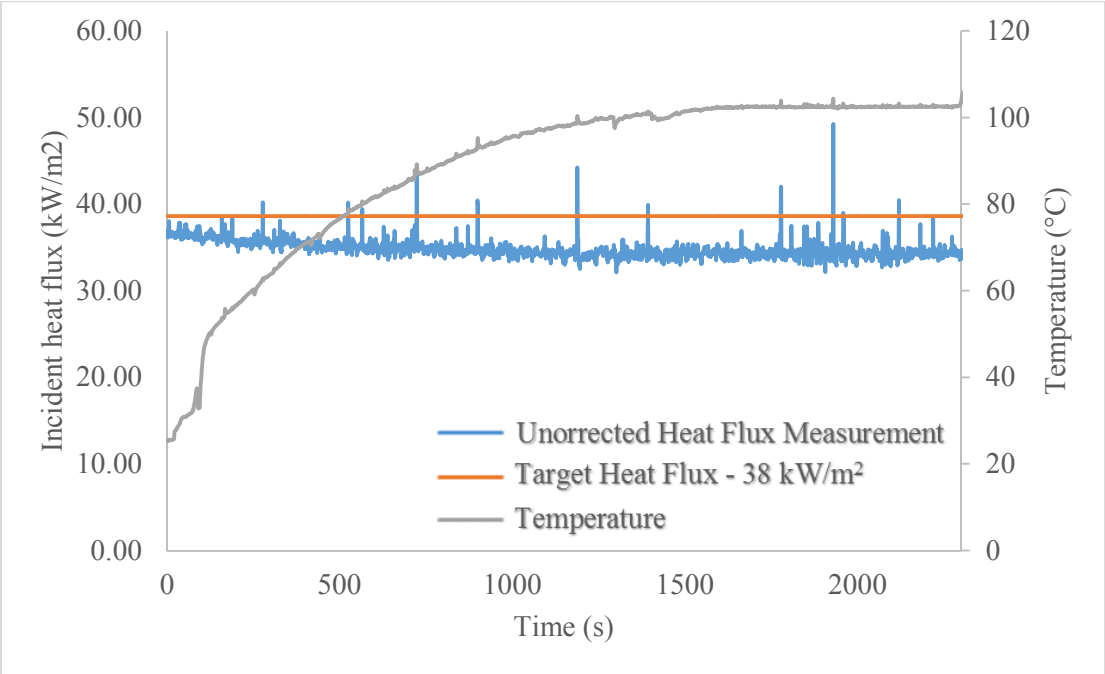

Figure 3.4 Uncorrected heat flux measurement using 1/8th inch Medtherm heat flux gauge

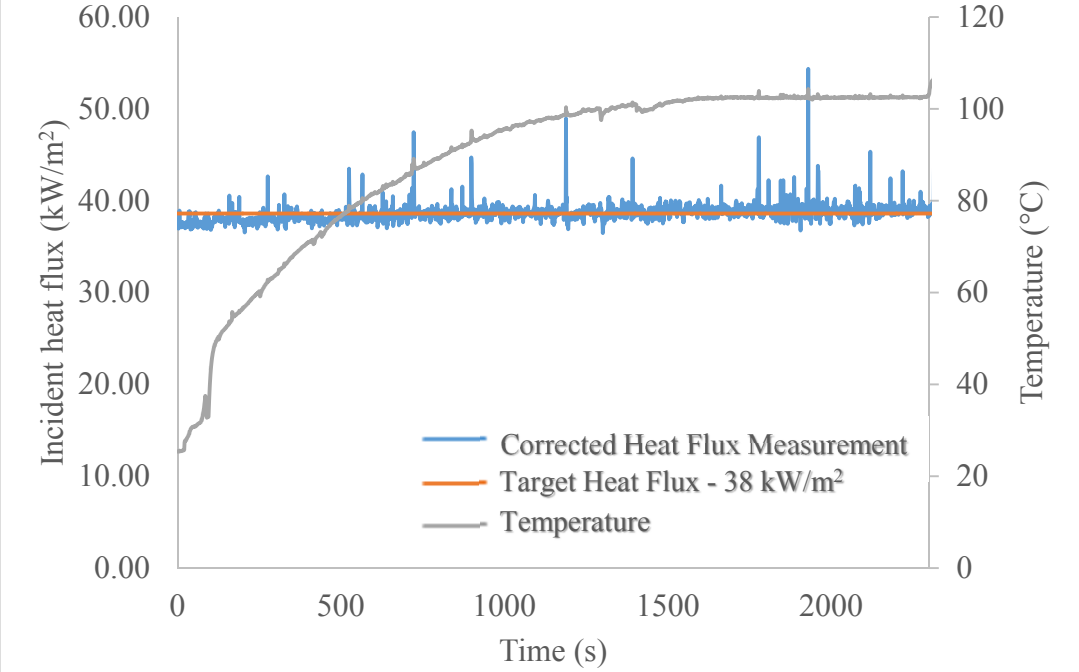

Figure 3.5 Corrected heat flux measurement using 1/8th inch Medtherm heat flux gauge

With measured or calculated convective coefficient on the surface of the gauge. The sensor can be calibrated and used without controlling the surface temperature by correcting for losses at the surface.

Chapter 4: Absorptivity and Emissivity Measurement of Burner and Heat Flux Gauge Paint Coatings

The burner and heat flux analysis requires the characterization of the paint absorptivity and emissivity. Emissivity is a measure of how well a body can radiate energy as compared with a blackbody. It is dependent on the body temperature, source wavelength, emission angle, and coating thickness. The calculation of energy loss from the surface requires emission into all direction and the averaged value of emissivity over all directions and wavelengths are sought after [15]. On the other hand, absorptivity is the fraction of incident energy absorbed by the surface. It is dependent on the directional and spectral characteristics of the incident radiation. Absorptivity is independent of the body temperature and the physical characteristics of the surface [15]. Full characterization of the paint is difficult and the coating surface needs to be assumed lambertian reflectance for simplicity. Three coatings were considered for use on burner and gauge surface selected mainly for ease of availability; Nextel Suede 3101 flat black, Rust-Oleum High-Heat, and Medtherm Co. P/N 20825 paint. These paints are characterized in two ways with heat flux gauge or copper disk.

4.1 Source spectrum and spectral emissivity examples

Careful consideration is made to the selection of paint used on the burner and heat flux gauge in order to withstand high degree of thermal degradation with minimal gas emission for both 1G and 0G testing. Originally Mankiewicz Nextel Velvet Coating 811-21, Figure 4.1, was planned to be used but it is no longer available. It has a listed absorptivity of 0.98 [16]. This coating is used by Medtherm Co. as comparison

references for total absorptance with the Medtherm P/N 20825 and Medtherm Co. P/N HT-2000. Willey et al. [1] characterized the total reflectivity of the paint in Figure 4.1. The coating is replaced with Nextel Suede Coating 3101 flat black. It is a two part coating that much be used in conjunction with Nextel Primer 5523 anthracite color to achieve optically black surface. When correctly applied, the coating has the same absorptivity of 0.98. During 1G BRE experiments using this paint, it was found to easily degrade under thermal and physical stress.

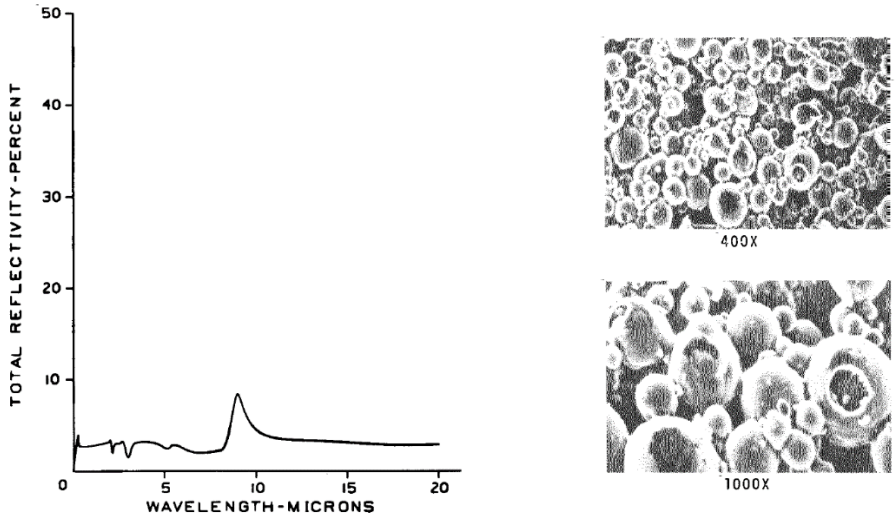

Figure 4.1 3M Nextel black velvet paint reflectivity and electron microscope image [1]

Rust-Oleum high heat flat black enamel spray paint's emissivity is characterized with thickness and temperature in a study done by Brian Lattimer [2]. The paint thickness was measured using a micrometer with a 0.00005 inch resolution. The emissivity was measured using a thermocouple attached to the surface of the painted specimen followed by using FLIR IR camera to adjust the emissivity value until the temperature reported in the IR camera matches the temperature of the thermocouple. The paint can be used with Rust-Oleum High Heat Primer for better adherence to the surface.

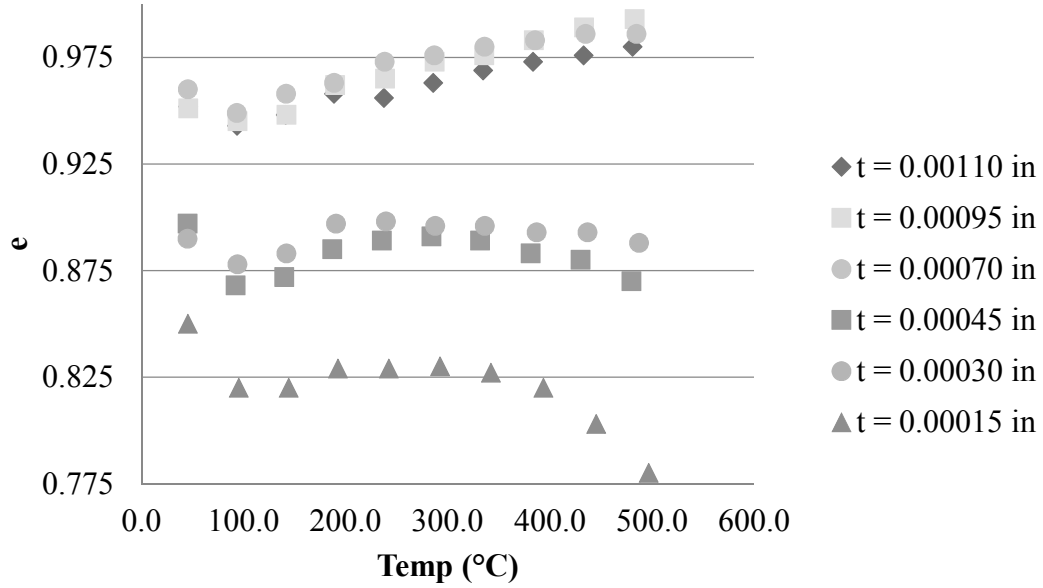

Figure 4.2 Lattimer: Rust-Oleum specialty high heat flat black enamel spray paint emissivity [2]

Zynolyte ® Hi-Temp paint can withstand temperatures up to 1200°F (538°C). The solar hemispherical absorptance is estimated to be 95.39% [3]. Other well characterized paints and coatings using Gier-Dunkle Integrating Sphere coatings specially formulated for aerospace applications are available on the market. But these formulations were difficult to obtain and was not fully considered for application to heat flux gauges and the BRE burner.

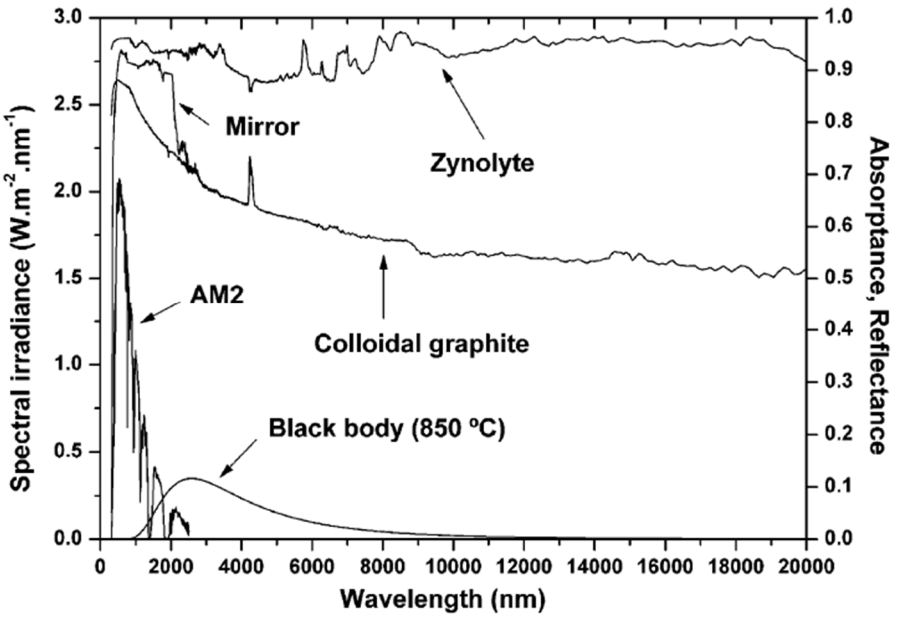

Figure 4.3 Zynolyte ® Hi-Temp paint absorptance at various source wavelengths [3].

4.2 Thermal degradation resistance testing

The resistance to thermal degradation and gas emission was tested using a very simple experiment. 3/8 inch thick copper plate was painted with the three paint in question: Nextel Suede 3101, Rust-Oleum High Heat, and Medtherm Co. P/N 20825. Figure 4.4, then subjected to maximum temperature of 300°C using a propane burner used in the calibration of the heat flux gauges. Type K insulated thermocouples were attached to the back of the plate to measure the temperature of the copper plate.

Figure 4.4 Paint sample after exposure to 300°C in the following order. Nextel Suede, Rust -Oleum, and Medtherm

After exposure to high temperature, qualitative observation was made to the state of the three paints. The Nextel Suede 3101 showed significant thermal degradation, the paint changed color to a rusted brown color and became powdery. Further, the paint showed significant off gassing as shown by oxidation pattern surrounding the paint. The Rust-Oleum paint showed no visible physical change. The Medtherm paint lost its physical integrity and was easily wiped off but showed no off gassing. From this simple test, Rust-Oleum paint was determined to have the best resistance to thermal degradation. However, unlike the Nextel Suede and Metherm paint, the absorptivity and emissivity of this paint was not characterized and must be found to be used on the sensor and burner surface.

4.3 Paint absorptivity measurement using heat flux gauge

Both the Nextel Suede 3101 and Medtherm paint was characterized and has a known absorptivity. These two paints were used as a check in two measurement methodology used. The paint absorptivity can be measured using heat flux gauges with the assumption that the absorbed calibration constant does not change with the surface

coating. The gauge surface and ambient temperature is made as equal as possible by circulating water from a reservoir subjected to ambient temperature for a long time. With $T_\infty = T_{surface}$, the heat balance on the surface of the gauge, the Equation 3.2 simplifies to,

$$CE = \alpha \dot{q_r''} \tag{4.1}$$

The measurement procedure is as follows,

1) Measure incident heat flux using a calibrated standard
2) Switch with a gauge with a known calibration constant but with an unknown paint and calculate absorptivity.

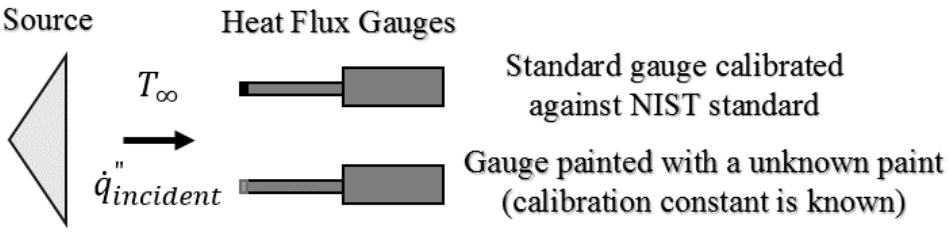

Figure 4.5 Determining absorptivity using heat flux gauges

In the case where the absorbed calibration constant and incident heat flux is known, the absorptivity of the can be calculated.

4.3.1 Measurement Samples

The one inch transfer standard, SN 180254, with an absorbed calibration constant of 11.77 kW/m^2 per mV was used to measure the incident flux. A 1/8th inch gauge, SN 180252, with an absorbed calibration constant of 15.35 kW/m^2 per mV was painted with different paint coatings. Various incident heat fluxes were used in the

experiment. The estimated absorptivity value were calculated by averaging all measured data.

#	180254 (V)	180252 (V)	180254 (°C)	180252 (°C)	T_∞ (°C)	$\dot{q}''_{incidnet}$	α
1	1.87E-03	1.46E-03	22.62	22.15	19.17	22.43	1
2	1.71E-03	1.34E-03	22.45	22.68	19.16	20.57	1
3	1.29E-03	9.75E-04	21.67	21.61	19.27	15.51	0.96
4	1.16E-03	9.16E-04	21.49	21.88	19.17	13.88	1.01
5	9.48E-04	7.18E-04	21.1	21.31	19.3	11.39	0.97
6	8.76E-04	6.85E-04	21.01	21.39	19.21	10.52	1
7	6.99E-04	5.23E-04	20.69	21	19.26	8.39	0.96
8	6.61E-04	5.12E-04	20.64	21.03	19.27	7.94	0.99
9	5.28E-04	4.03E-04	20.43	20.84	19.3	6.35	0.98
10	5.13E-04	3.88E-04	20.4	20.82	19.2	6.17	0.97
11	4.37E-04	3.24E-04	20.27	20.65	19.08	5.24	0.95
12	4.20E-04	3.19E-04	20.27	20.71	19.04	5.04	0.97

Table 4.2 Nextel Suede 3101 absorptivity measurement, $\alpha = 0.98$

#	180254 (V)	180252 (V)	180254 (°C)	180252 (°C)	T_∞ (°C)	$\dot{q}''_{incidnet}$	α
1	1.75E-03	1.26E-03	23.08	23.04	21.08	21.03	0.92
2	1.66E-03	1.21E-03	23.22	22.73	20.97	19.9	0.93
3	1.23E-03	8.83E-04	21.74	21.6	21.05	14.75	0.92
4	1.14E-03	8.26E-04	21.69	21.35	21.07	13.65	0.93
5	1.22E-03	8.69E-04	21.82	21.86	20.96	14.65	0.91
6	1.13E-03	8.17E-04	21.94	21.61	21.05	13.53	0.93
7	9.43E-04	6.69E-04	21.62	21.82	21.03	11.33	0.91
8	8.97E-04	6.53E-04	21.79	21.81	20.95	10.77	0.93
9	9.42E-04	6.68E-04	21.73	21.93	21	11.31	0.91
10	8.95E-04	6.47E-04	21.9	21.91	20.97	10.75	0.92
11	6.55E-04	4.70E-04	21.43	21.57	21.01	7.86	0.92
12	6.54E-04	4.54E-04	21.44	21.55	21.01	7.85	0.89

Table 4.3 Rust-Oleum specialty high heat flat black enamel spray paint absorptivity measurement, $\alpha = 0.91$

#	180254 (V)	180252 (V)	180254 (°C)	180252 (°C)	T_∞ (°C)	$\dot{q}''_{incidnet}$	α
1	1.91E-03	1.38E-03	22.38	21.33	19.57	22.99	0.92
2	1.64E-03	1.20E-03	21.9	22.02	19.58	19.64	0.94
3	1.30E-03	9.26E-04	21.29	20.86	19.46	15.66	0.91
4	1.11E-03	8.17E-04	20.97	21.17	19.55	13.3	0.94
5	9.45E-04	6.57E-04	20.64	20.5	19.62	11.35	0.89
6	8.34E-04	6.16E-04	20.5	20.67	19.58	10.01	0.94
7	7.07E-04	4.99E-04	20.25	20.24	19.61	8.49	0.9
8	6.47E-04	4.71E-04	20.17	20.33	19.59	7.76	0.93
9	4.41E-04	3.11E-04	19.75	19.88	19.41	5.29	0.9
10	4.12E-04	2.98E-04	19.73	19.9	19.57	4.95	0.93
11	3.65E-04	2.55E-04	19.63	19.74	19.52	4.38	0.89
12	3.42E-04	2.44E-04	19.6	19.78	19.51	4.11	0.91

Table 4.4 Medtherm P/N 2082 absorptivity measurement, $\alpha = 0.92$

The measurement result is shown in Table 4.1.

Paint	**Absorptivity (Heat Flux Gauge)**
Nextel Suede 3101	0.98
Medtherm Paint	0.92
Rust Oleum Hi-Heat Paint	0.91

Table 4.1 Measured absorptivity using heat flux gauge method

4.4 Paint absorptivity and emissivity measurement using copper disk calorimeter

Both absorptivity and emissivity of the coating can be measured using a copper disk. Essentially a copper slug calorimeter, heat transfer rate is examined to obtain the two values in question. A copper disk of diameter 1.5 inch was made and painted on both faces with the paint with unknown absorptivity and emissivity. The copper disk is insulated around the edge to reduce the convective losses and to limit the radiant exposure to only the faces. Two thermocouples were attached to the copper disk at the center and near the edge by hammering into a pre-drilled hole, Figure 4.6.

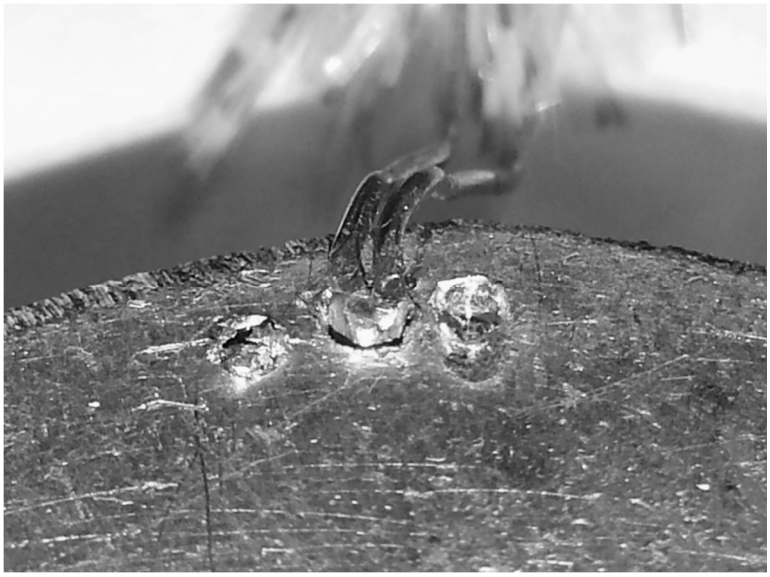

Figure 4.6. Hammered in thermocouple near the edge.

To prevent further heat loss, the thermocouple are also used to hold up the copper disk to the radiant heater, Figure 4.7.

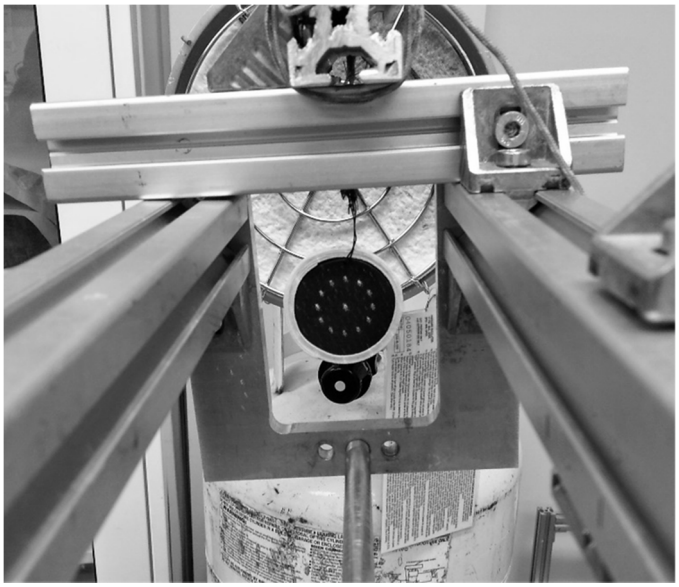

Figure 4.7. Painted copper disk held up to the heater using thermocouple with laser guide from pyrometer

An Omegascope Handheld Infrared Thermometer OS533E pyrometer with a spectral response between 8 to 14 μ with variable emissivity setting was setup with view angle to only observe the copper disk. Figure 4.8 shows the copper disk measurement schematic.

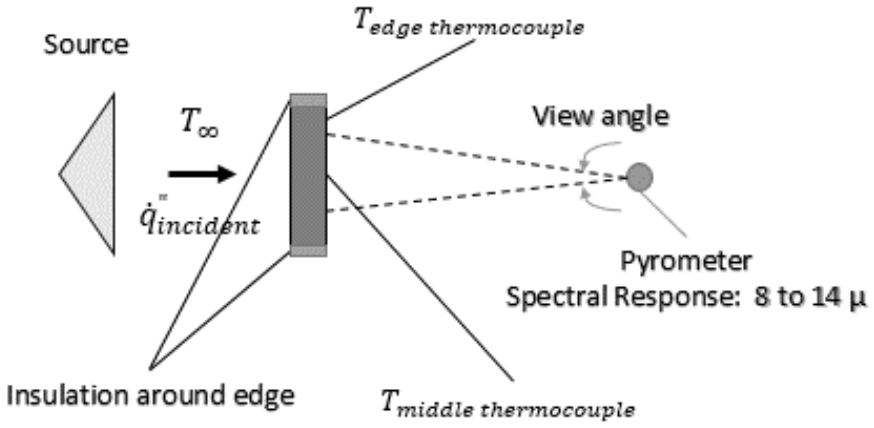

Figure 4.8 Painted copper disk measurement diagram

The experimental setup is shown below in figure 4.9.

Figure 4.9. Copper disk measurement setup

Heat balance on the surface of the copper disk shows,

$$m_{cu}c_{cu}\frac{dT}{dt} = \alpha\dot{q}_i^{"} - 2h(T_{cu} - T_\infty) - 2\epsilon\sigma(T_{cu}^4 - T_\infty^4) \tag{4.2}$$

During the initial response of the copper disk to a radiant heat source, the temperature of the copper and ambient is assumed to be equal. The model for the initial response is simply,

$$m_{cu}c_{cu}\left(\frac{dT}{dt}\right)_{t=0} = \alpha\dot{q}_i^{"} \tag{4.3}$$

The absorptivity of the copper disk can be calculated in terms of the mass, specific heat of copper, and the initial temperature rise if the incident heat flux to the face is known. The equation can be further modified to obtain convective heat transfer coefficient on the surface of the copper disk. With the removal of the radiant source and calculation of h gives,

$$h = \frac{-\frac{m_{cu}c_{cu}\frac{dT}{dt}}{Area} - 2\epsilon\sigma(T_{cu}^4 - T_\infty^4)}{2(T_{cu} - T_\infty)} \tag{4.4}$$

The pyrometer with variable emissivity setting is used to measure the emissivity of the paint.

$$\epsilon\sigma T_{cu}^4 = \epsilon\sigma T_{pyrometer}^4 \tag{4.5}$$

The emissivity of the pyrometer is set at 1 and the above equation simplifies to,

$$\epsilon = \left(\frac{T_{pyrometer}}{T_{cu}}\right)^4 \tag{4.6}$$

The measurement is conducted using the heat flux calibration apparatus. The rotatable heat flux holder was used with a water cooled 1 inch diameter Medtherm heat flux gauge to measure the incident heat flux from the radiant heater then removed out of sight. In turn, the copper disk is placed in the location where the heat flux gauge is located, Figure 4.10.

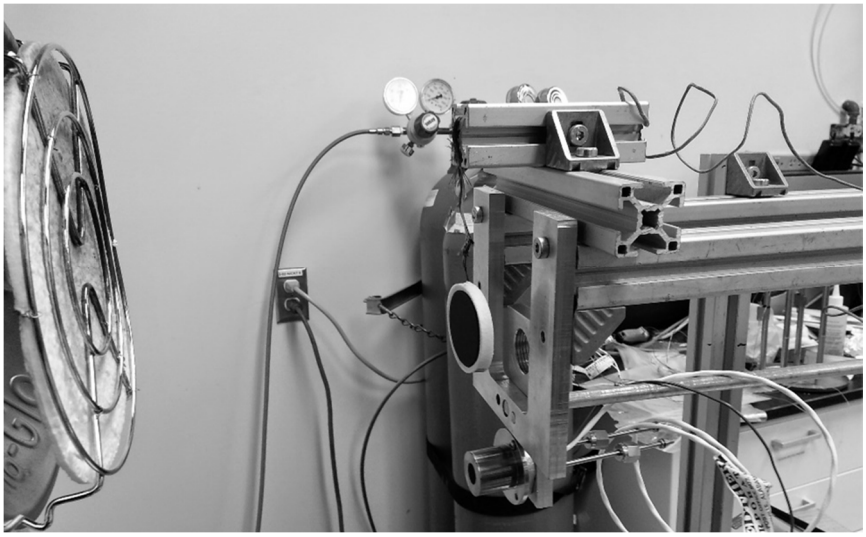

Figure 4.10 Heat flux gauge and copper disk location in calibration apparatus

4.4.1. Copper disk measurement samples

Experiment with copper disk painted with Nextel 3101 is examined. First, the heat flux is measured using water cooled Medtherm 1 inch transfer standard, SN 180254, with absorbed calibration constant of 11.77 kW/m^2 per mV. The measured heat flux is 8.653 kW/m^2. The temperature rise of the copper disk positioned like Figure 4.11 is shown below.

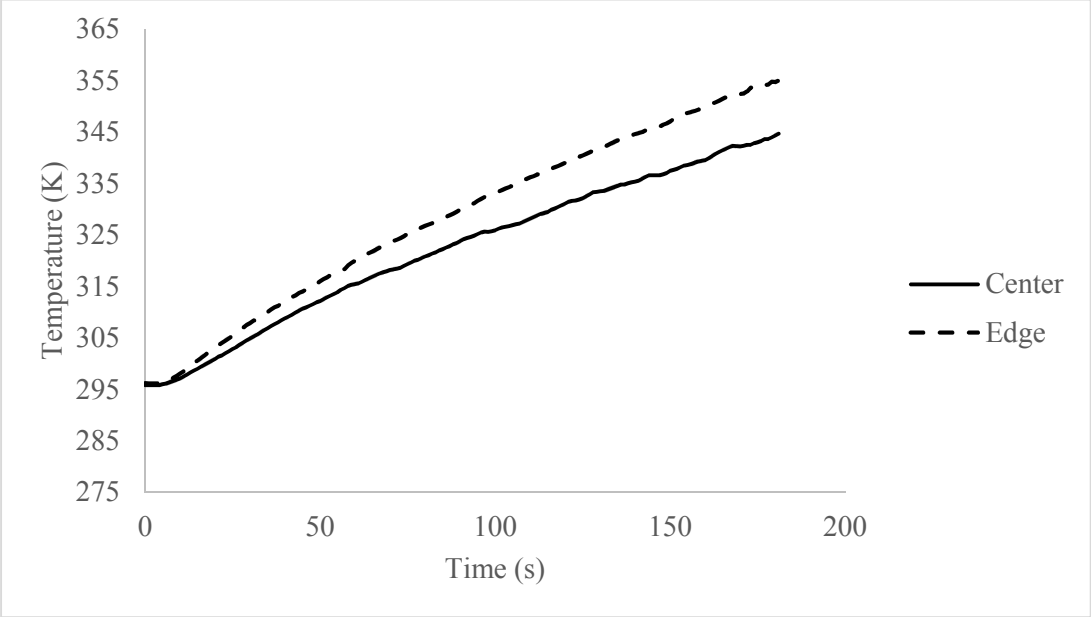

Figure 4.11 Temperature rise of the copper disk painted with Nextel 3101 Suede coating.

The initial temperature rise of the copper disk is of interests and the corresponding slope is found. The specific heat of copper is assumed constant, c_{294K}=0.385 J/g/K. The mass of the disk is 71.55 g with surface are of 0.00145 m^2. Equation 36 is applied and the absorptivity of the coating is found to be 0.98 using the edge thermocouple and 0.73 using center thermocouple.

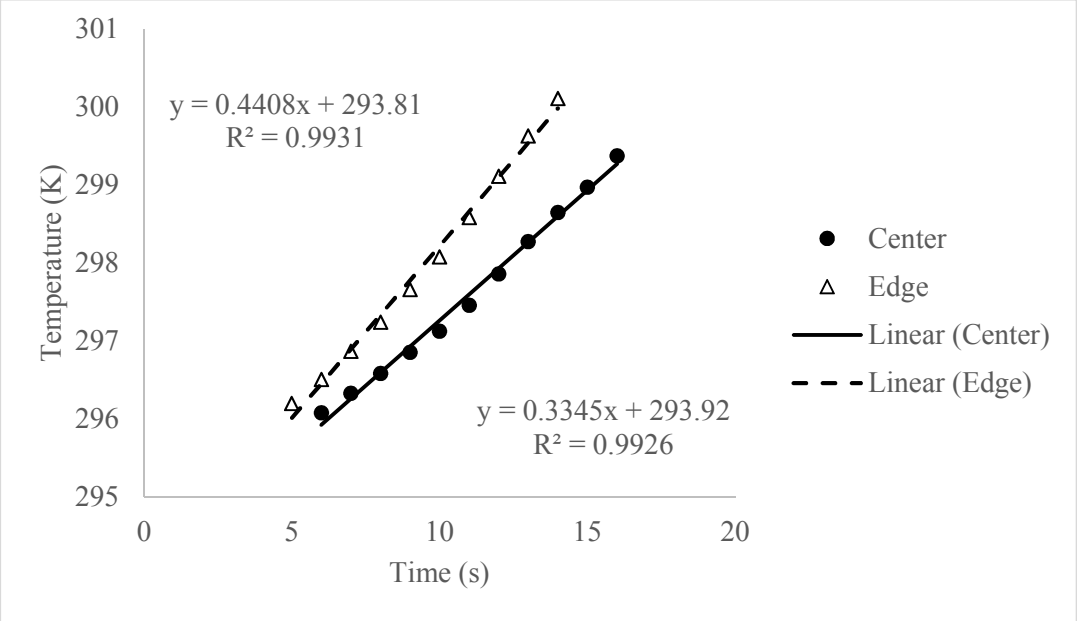

Figure 4.12 Initial temperature rise of the copper disk

The both emissivity and the convective heat transfer coefficient is found by letting the copper disk cool. Equation 39 is applied to Figure 4.13.

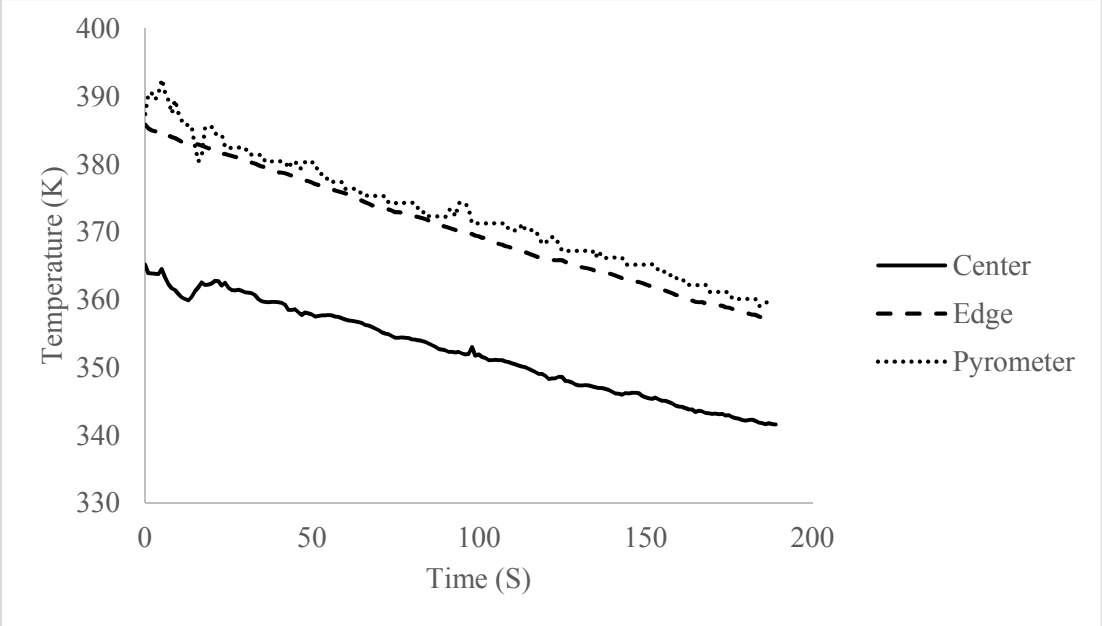

Figure 4.13 Temperature decrease of copper disk and pyrometer measurement.

The temperature difference measured between the center and edge thermocouple differs by 20°C when cooling. For emissivity calculation, data from the edge thermocouple was used along with the pyrometer. The calculated emissivity value is averaged and found to be ~1. The calculated result using the copper slug calorimeter is as follows,

Paint	Emissivity	Absorptivity (Copper Slug)
Nextel Suede 3101	~1	0.98
Medtherm Paint	~1	0.92
Rust Oleum Hi-Heat Paint	~1	0.95

Table 4.5 Measured absorptivity using copper disk method

The derivative of the temperature decrease is found and shown in Figure 4.14.

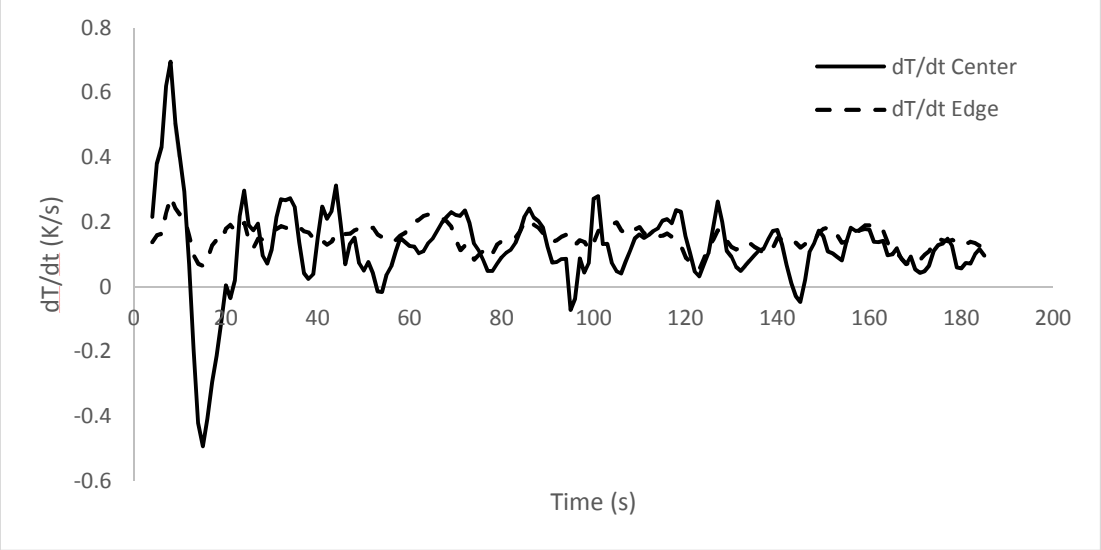

Figure 4.14 Derivative of the temperature decrease over time.

The slope of the temperature decrease is roughly constant over the measurement. For simplicity of the calculation, the convective coefficient was assumed to be constant. The convective coefficient was calculated using Equation 4.4 with an averaged dT/dt and found to be approximately 10.7 W/m^2K. A model was created using Equation 35

to check the calculated values, Figure 4.15 and Figure 4.16 The highest percent error is ~1%.

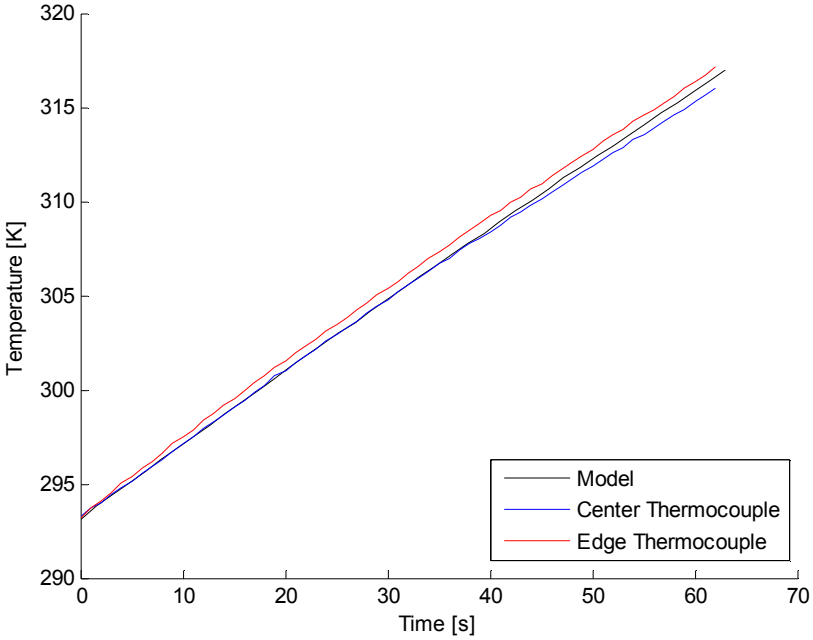

Figure 4.15 Temperature evolution model for temperature rise

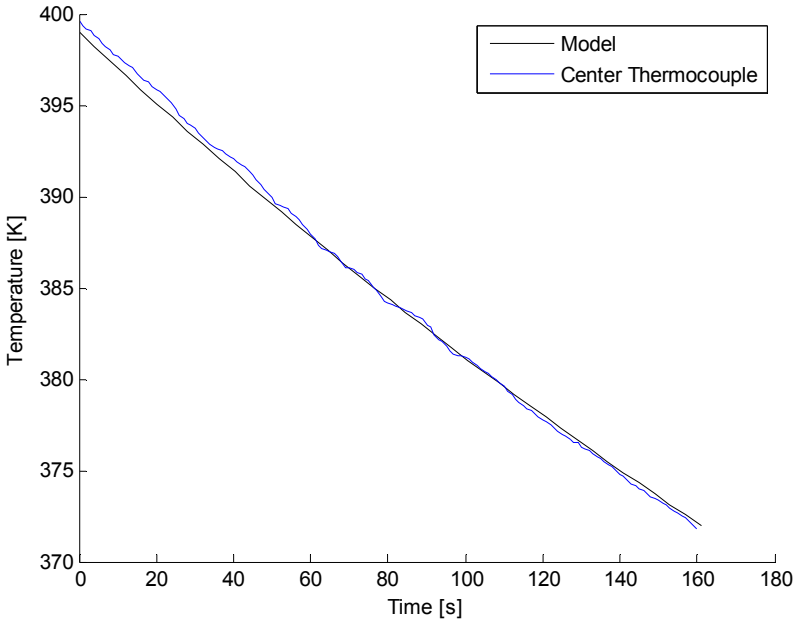

Figure 4.16 Temperature evolution model for cooling

Chapter 5: Apparatus to Measure Flame Radiation

The flame radiation is an important quantity of flame heat transfer to the surface. If radiation loss is greater than the chemical energy, flame cannot sustain itself. A flame radiation fraction, X_r is defined. It is a dimensionless group characterized by a fraction of radiant energy lost with respect to the actual chemical energy release from the flame [11].

$$X_r = \frac{\dot{q}_r}{\dot{Q}} = \frac{4\pi R^2 \dot{q}_R^{"}}{\Delta H_c \dot{M}_F} \tag{5.1}$$

This X_r acts as an important parameter in CFD models such as FDS for local flame predictions [17], and is used to compute total radiation from large pool fires [18]. The radiation fraction is not constant for a given fuel as the fire grows in size. It decreases with larger diameter pool fire due to soot blockage. Lower values are also expected with small and laminar flames due to relatively smaller amount of soot. However, the radiant fraction should remain constant for turbulent flame. Due to the importance of flame radiant fraction for free burning, it is measured in the experiments with the BRE burner for further study.

5.1 Radiometer construction and Calibration

In order to obtain a better understanding of the role of radiation in the burning rate emulation experiment, a radiometer using a thermopile type sensor was specially built and calibrated to measure the flame radiant fraction X_r. Radiation fraction can be measured using various methods. Medtherm's Gardon or Schmidt-Boelter thermopile type sensor can be specified with a window attachment to eliminate convective heat transfer to only measure the radiation with sapphire as a standard window material [13].

The measurement with Medtherm heat flux gauges offer very slow response of 0.25 seconds. Medtherm gauges provide poor control of viewing angle and ensuring that the gauge only see the flame and not the burner body is difficult. A custom radiometer was opted to be built due to the slow response of the Medtherm sensor and problem with its view angle.

5.1.1. Sensor Selection

Dexter 1M thermopile detector was selected to be the sensing thermopile for the radiometer. It is a thin film-based thermopile with an active sensing area of 1.0 mm that provides a linear signal output from 10^{-6} to 0.1 W/cm^2 with 32 ms response time. In addition, a BaF2 window was custom specified in order to obtain a flat spectral response between 100 nm to 100 μm. Since the sensor output voltage is very small, the sensor output is routed to a 9 volt Dexter Research 1010 low noise amplifier before it is connected to a Fluke Data Acquisition System. The thermopile detector is contained in a TO-5 package that is easily soldered in to BNC male or female connection. The schematic of the sensor is shown in Figure 5.1 and 5.2.

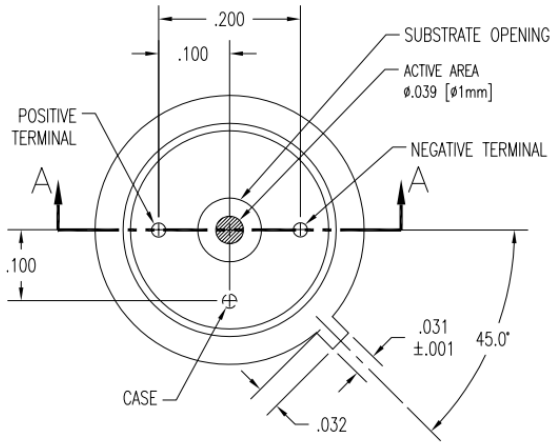

Figure 5.1 Dexter 1M thermopile detector schematic top view [4]

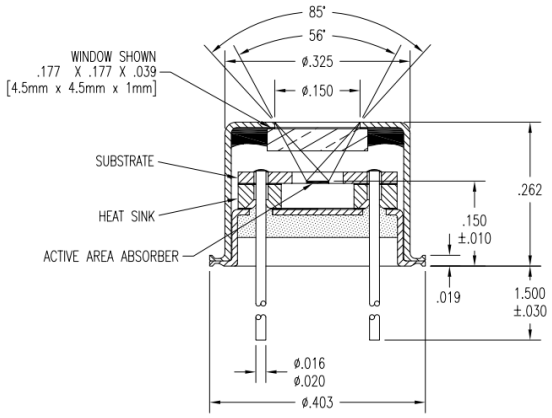

Figure 5.2 Dexter thermopile detector schematic cross section view [4]

The sensor element's view angle is largely dependent on the glass window size and the substrate opening size, with larger opening resulting in larger view angles. The sensor used in the experiment was custom ordered with specific window and substrate opening sizes to accommodate the largest anticipated flame height from the BRE burner.

5.1.2. Radiometer housing and construction

The sensor housing is assembled using Thorlab three 1 inch diameter aluminum lens tubes. In addition, three 1 inch diameter Thorlab aluminum optic adapter was used in assembly to serve as a holders for the sensor element and BNC outlet as well as to serve as a ground source for the sensor. To ensure that the sensor was properly aligned, the optic adapter was customized by boring a hole and press fitting a TO-5 adapter to be flushed before installing the 1M detector, Figure 5.3.

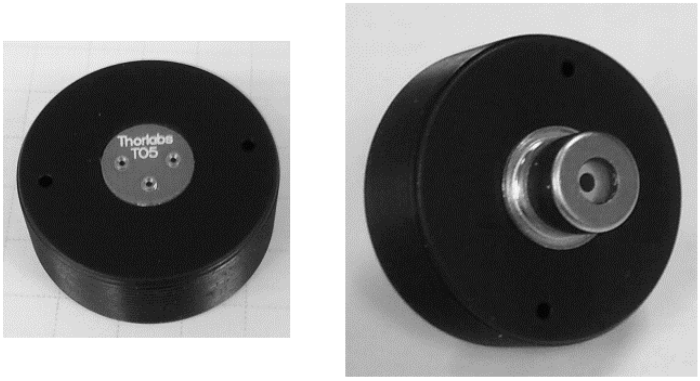

Figure 5.3 Installation of TO-5 adapter and 1M detector

A Thorlab 1 inch stainless steel diaphragm shutter is attached on the front of the body. It has two main purposes. First, it protects the sensor when the radiometer is not in use. Second, by exposing the stainless steel shutter to the sensor, the radiometer is able to check for drift in measurements. The radiometer body could potentially increase in temperature when exposed to high flame radiation. In response, the sensor output could drift due to radiation from the sensor housing itself. The stainless shutter is assumed to be approximately equal to the sensor housing temperature. By measuring with the shutter closed, the drift in the sensor output can be determined and the overall measurement is properly corrected. A schematic of the radiometer including the writing is shown in Figure 5.4.

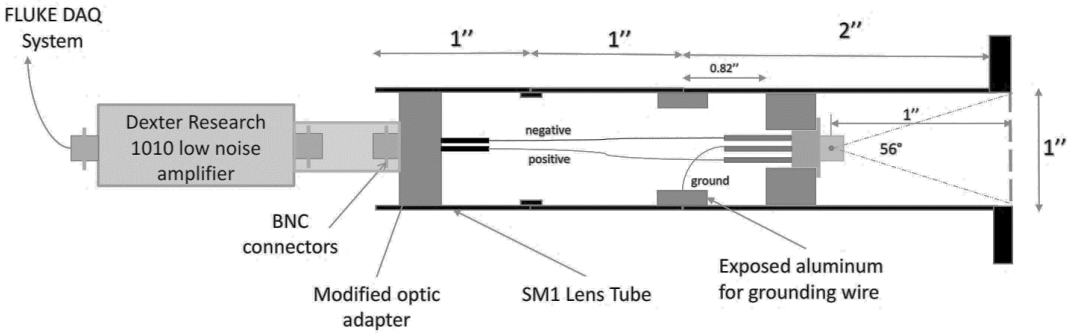

Figure 5.4 Radiometer schematic

Two extra precautions were taken to ensure accurate radiation measurement using the radiometer. A cold wall was made using a sheet metal painted with a high absorptivity paint to prevent radiometer from picking up reflected radiation. The forward facing part of the diaphragm is covered with an aluminum foil to minimize the sensor housing from heating up via flame radiation.

5.1.3. Radiometer calibration

The radiometer is calibrated using Newport Blackbody Furnace as a heat source. The radiometer calibration setup is shown in Figure 5.5.

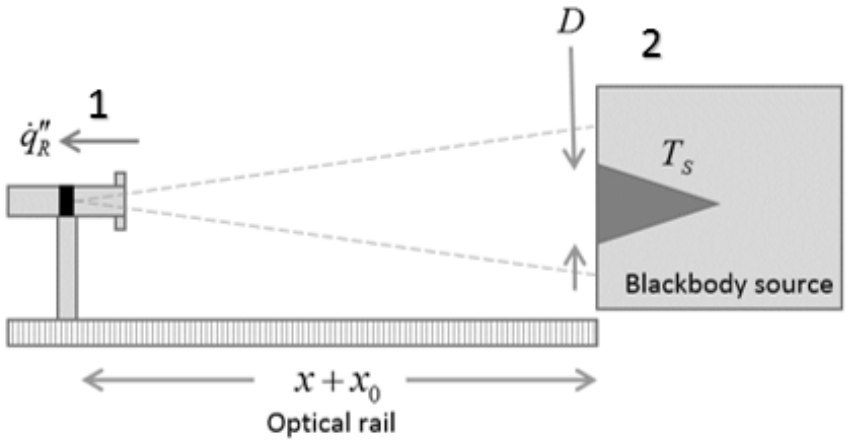

Figure 5.5 Radiometer calibration setup

The view factor from the radiometer to the blackbody source is assumed to be a point seeing a disk. Then the view factor from the blackbody to the sensor is,

$$F_{12} = \frac{D^2}{D^2 + 4(x + x_o)^2} \tag{5.1}$$

Heat balance is then applied to the sensor. The resulting equation is,

$$\dot{q}_R^{"} = C * V = \frac{\pi D^2 \epsilon \sigma (T_S^4 - T_\infty^4)}{4\pi (x + x_0)^2} \tag{5.2}$$

The calibration constant for the radiometer is then obtained by plotting the inverse square of voltage against different ranges of distances,

$$\frac{1}{V^{\frac{1}{2}}} = \sqrt{\frac{4C}{D^2\epsilon\sigma(T_S^4 - T_\infty^4)}}(x + x_0) = a(x + x_0) \tag{5.3}$$

Since the slope is not dependent on the value of x_o, the calibration constant for the radiometer is solved,

$$C = \frac{1}{4}a^2D^2\epsilon\sigma(T_s^4 - T_\infty^4) \tag{5.4}$$

The calibration of the radiometer was done at relatively high blackbody temperatures ranging from 1000°C to 1150°C. The calibration did not succeed at lower temperatures and gave erroneous results because the low radiation level was affected too much by distance. Between 1000°C and 1150°C, total of 4 measurements were taken with the radiometer at 4 different distances, the resulting plot is shown below.

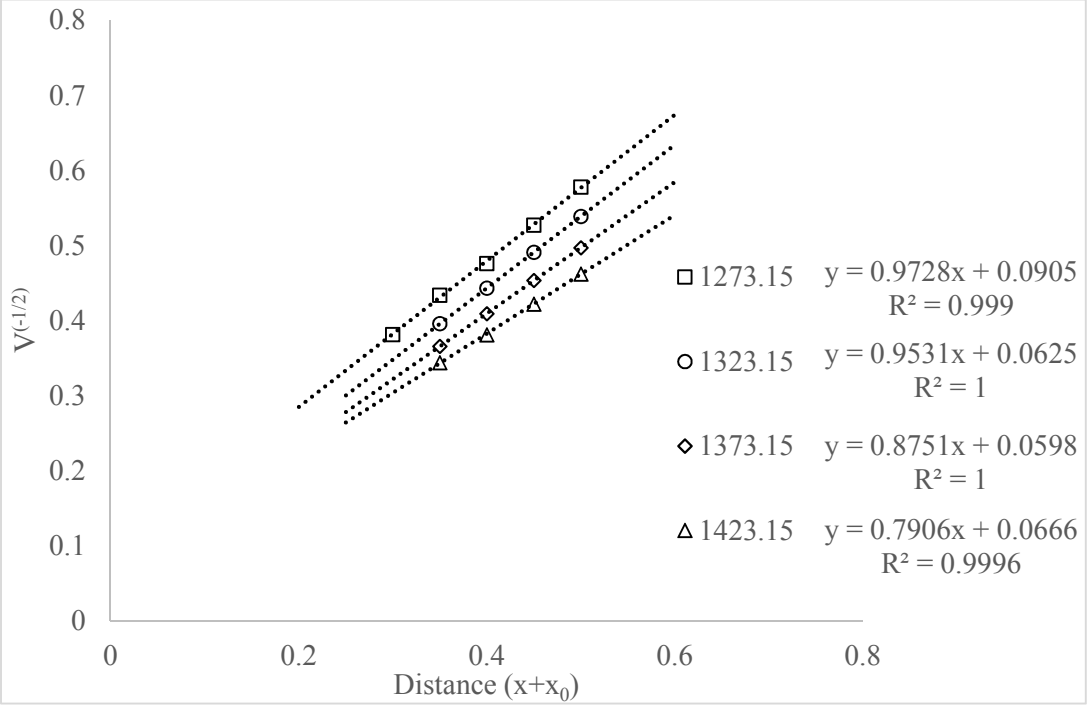

Figure 5.6 Radiometer calibration data

Four different calibration constant was calculated using equation 5.4, then averaged together. The calibration constant for the constructed radiometer was found to be 0.0024 kW/m^2V.

5.2 Radiometer measurement samples

Care was taken so that the radiometer only views the flame themselves and not the burner. This was ensured by checking the view angle of the sensor by utilizing a small lighter flame across the sensor view.

Prior to measurements with the radiometer, a zero value is established by exposing to the sensor to a cold burner with no flame. The zero value observed where the apparatus was setup was between -0.016 to 0.01 volts. Then the radiometer is exposed to a given flame and occasionally close the shutter to check the zero value for a brief moment to ensure that the sensor measurement has not drifted. During the course of the measurement, the measurement did no shift. Figures 5.7 and Figure 5.8 show radiometer measurement samples at different fuel heat release rate using pure propene.

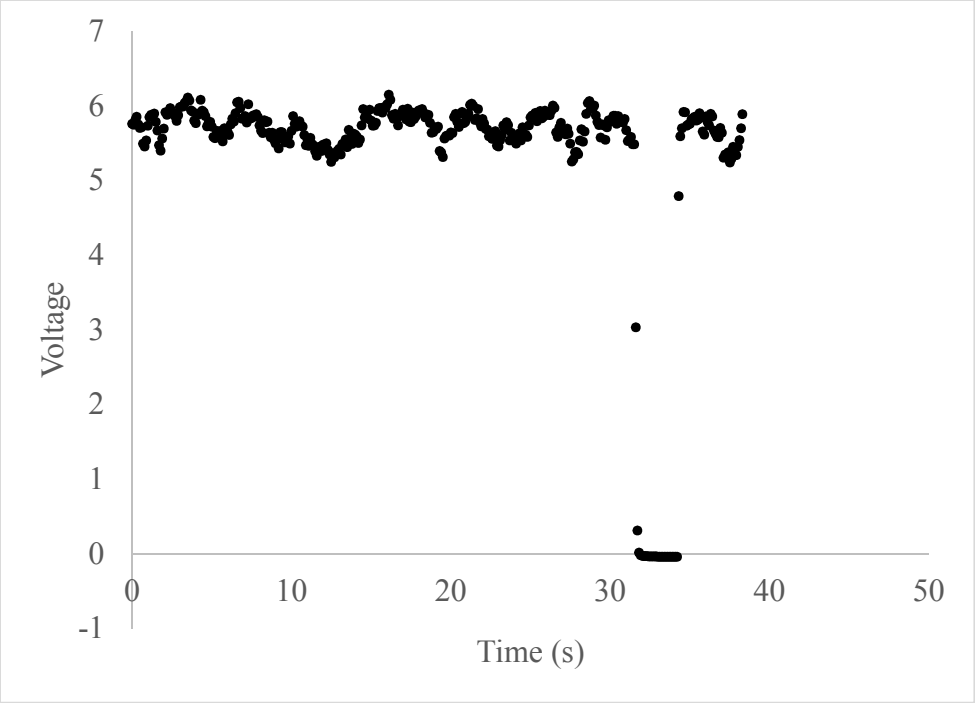

Figure 5.7 0.43 kW propene flame measurement at distance of 0.24 m

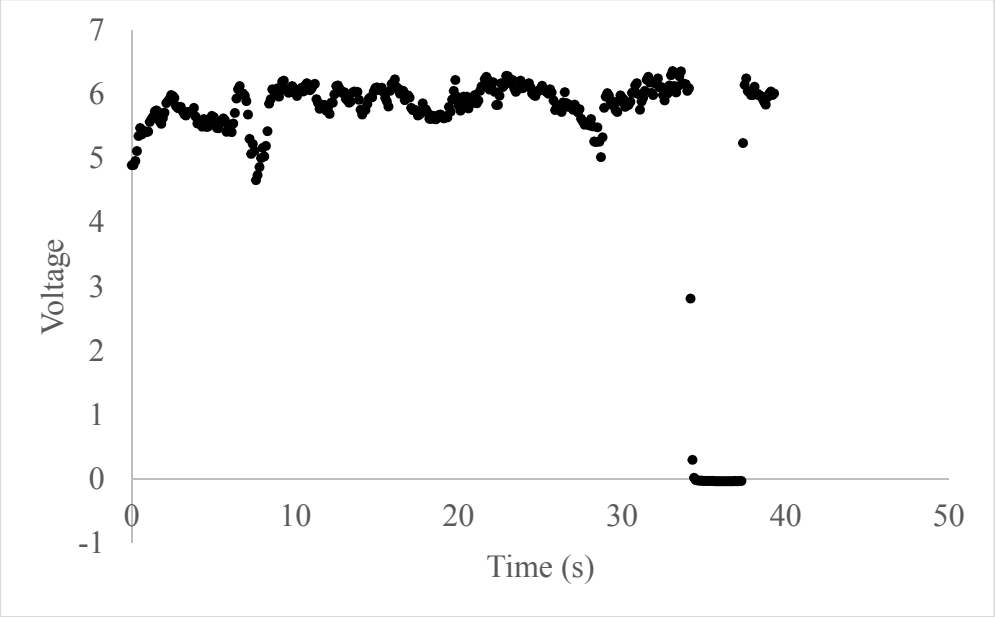

Figure 5.8 2.4 kW propene flame measurement at distance of 0.59 m

The equation to calculate radiant fraction is as below,

$$\mathrm{X}_r = \frac{\dot{q}_r}{\dot{Q}} = \frac{4\pi R^2 \dot{q}_R^{"}}{\Delta H_{c,mixture} \dot{M}_F} \tag{5.5}$$

Where,

$$\dot{q}_R^{"} = C * V \tag{5.6}$$

The $\dot{M}_F$ is the total mass flow rate which comprises of fuel and inert gas mixture. $\Delta H_{c,mixture}$ is heat of combustion of mixture of fuel and inert gas. It is calculated by using the theoretical heats of combustion. The radiometer measurement is averaged for a total of 30 seconds.

Chapter 6: Application of BRE Burner

6.1 Mapping steady burning domain as a function of four properties

The BRE can be used to establish the burning conditions for condensed fuels using two gas mixtures as a function of four fuel properties. The emulation of condensed fuel is dependent on the heat of gasification of the material, heat of combustion, re-radiation heat flux, and flame radiation. Methane burning with nitrogen dilution is examined as an application to the steady burning theory.

The corresponding heat of gasification can be found using the heat flux sensor measurement is,

$$L = \frac{\dot{q}''_{net}}{\dot{m}''} \tag{6.1}$$

Where,

$$\dot{q}''_{net} = CE + \epsilon\sigma(T_H^4 - T_s^4) + h_B(T_H - T_s) \tag{6.2}$$

The Alicat mass flow controllers were used to control the fuel and diluent flow rate up to 2 LPM. Omega series 5000 rotameters calibrated with bubble flow meter are used for flow rate above 2 LPM.

The local heat flux is measured in the burner surface at two local points at center and 15 mm away from the center. The net heat flux must be found by averaging the two local measurement with a distribution. The center and edge heat flux measurement are taken with a 1/8th inch Medtherm heat flux gauge without water cooling. The surface of the gauge and the burner is painted with Rust-Oleum Hi Temp paint. Figure 6.1 and

6.2 shows the heat flux measurements for methane with nitrogen dilution between 0 to 1.80 LPM

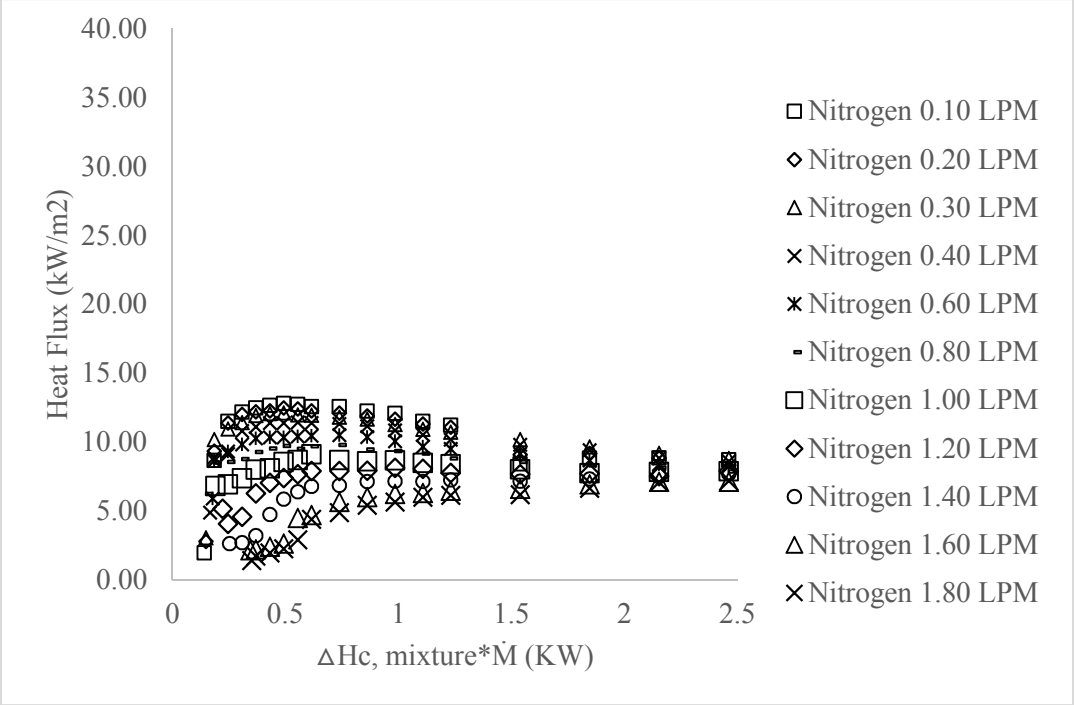

Figure 6.1 Center heat flux gauge measurement with h_B correction

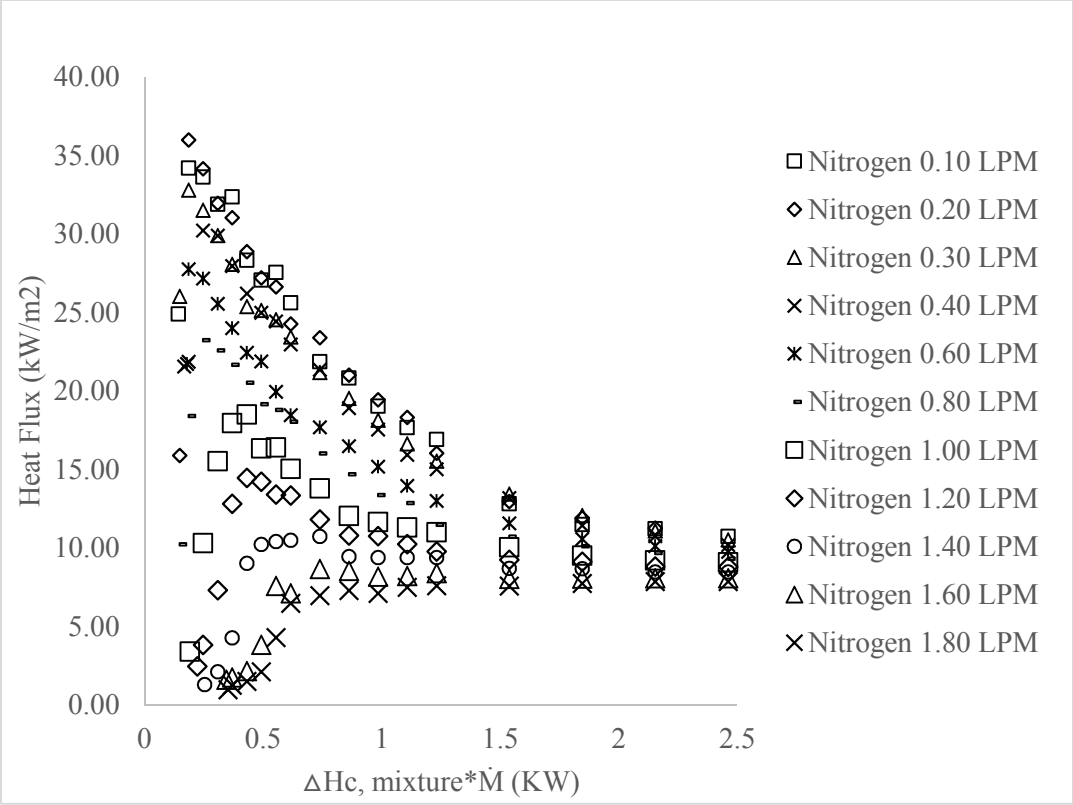

Figure 6.2 Edge heat flux gauge measurement with h_B correction

Attempted characterization of the complete heat flux distribution of the BRE burner was done by modifying the brass screen burner to measure heat flux gauges at 0, 5, 10, 15, 20, and 22 mm from the center.

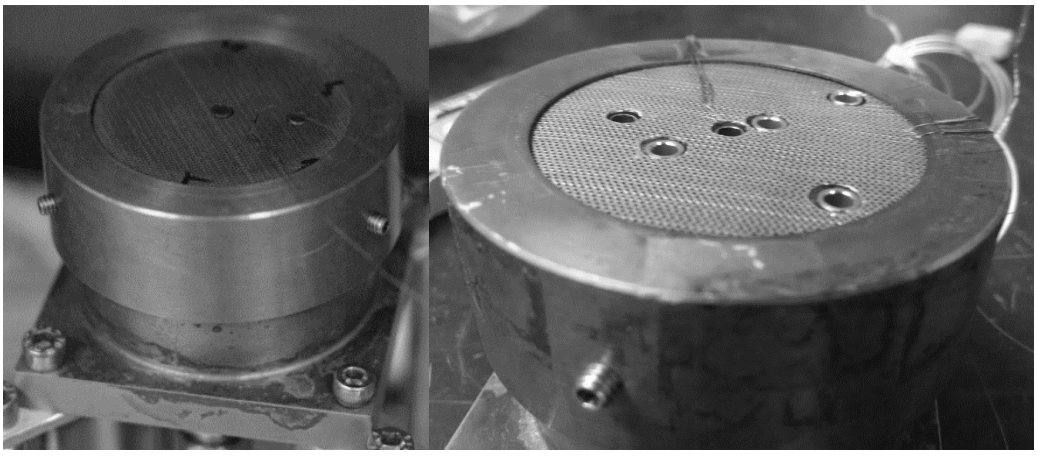

Figure 6.3 Brass scree burner modification

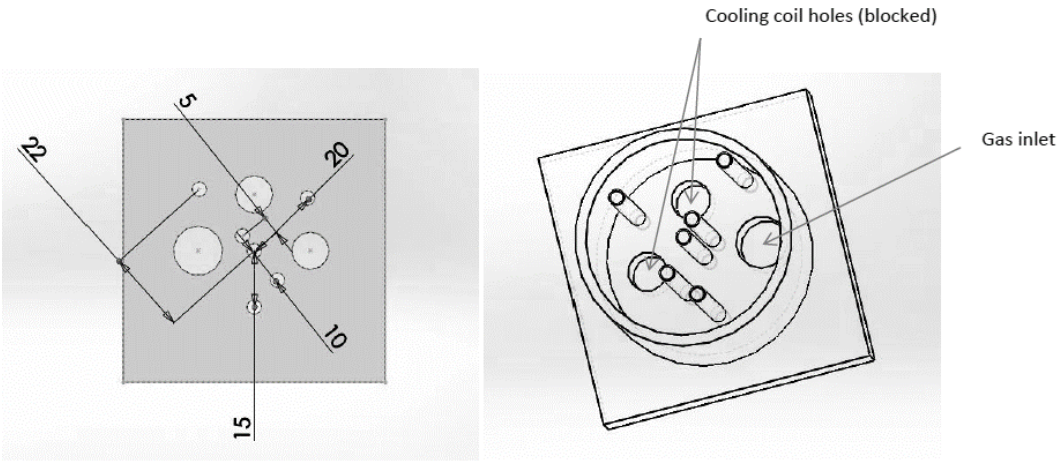

Figure 6.4 Brass burner modification schematic

The heat flux was measured using methane and ethylene at heat release rate of 0.37, 0.74, and 1.85 kW. The results are shown in Figure 6.5 and 6.6.

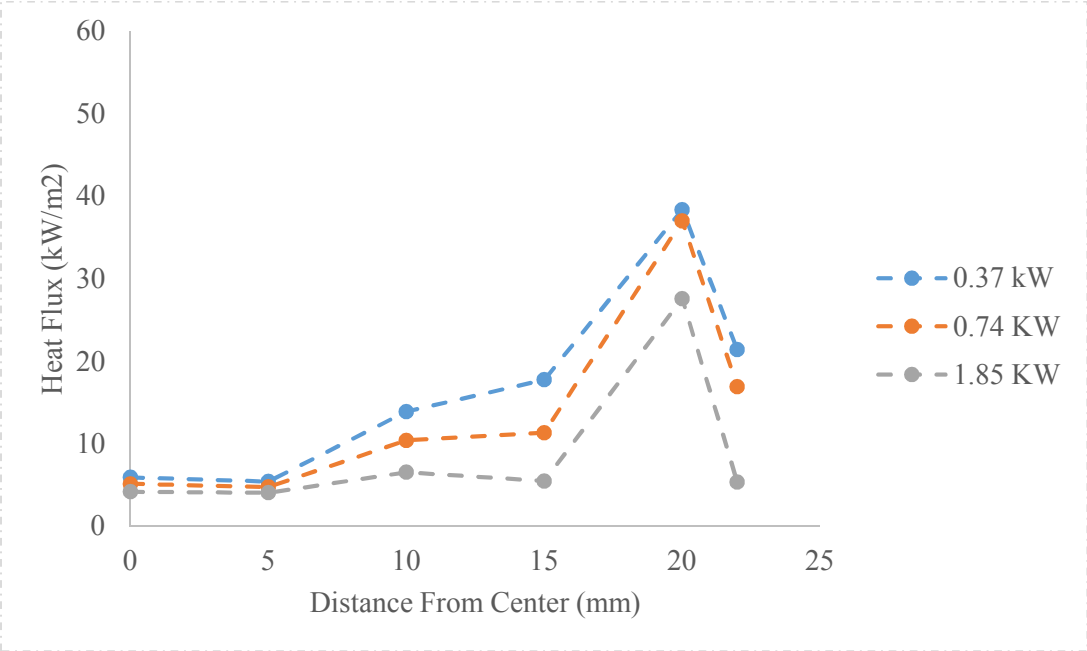

Figure 6.5 Pure methane heat flux distribution using brass screen burner

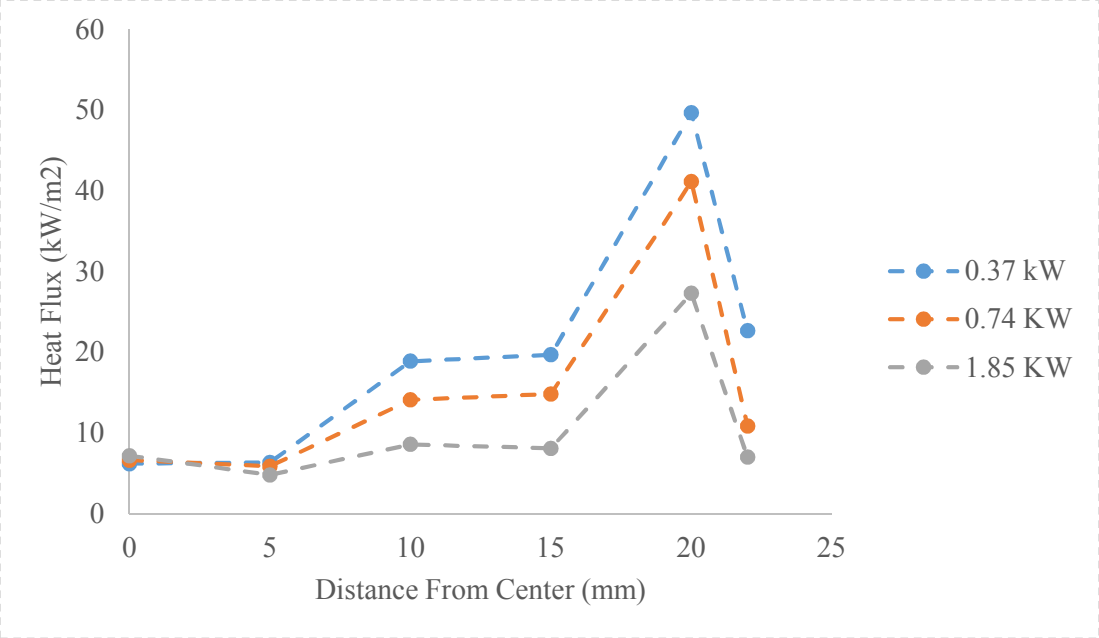

Figure 6.6 Pure ethylene heat flux distribution using a brass screen burner

Estimated averaged net heat flux into the surface is calculated by integrating the distribution over the surface. The obtained overall heat flux into the surface is then used to calculate heat of gasification using Equation 6.1 and Equation 6.2. The previous step change assumption was used to average the heat flux distribution. The result can be plotted with heat of combustion of mixture, Figure 6.7. The measured heat flux distribution will be applied after further analysis.

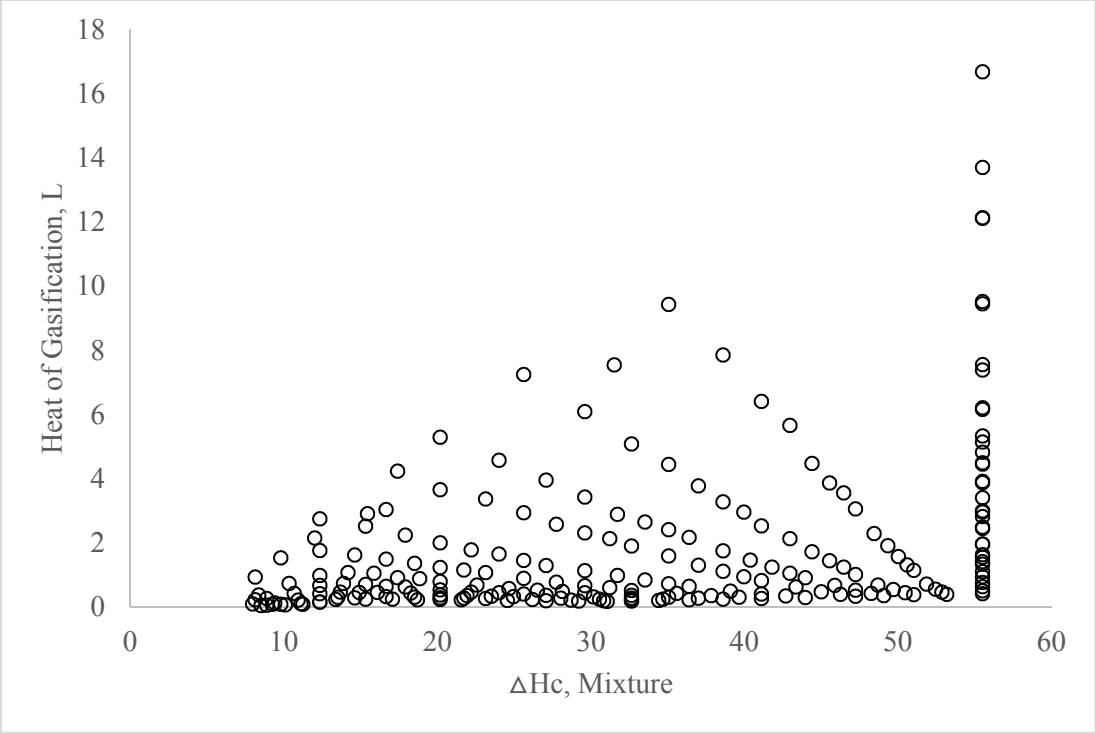

Figure 6.7 Heats of gasification

The charring materials lie outside of the domain plotted in Figure 6.7. These materials need external heat flux or increased ambient oxygen concentration in order to sustain steady burning. Liquid fuels and non-charring solids are expected to fall within the flammability domain. Further study is ongoing on how to present the data with explanation and verification.

6.2 BRE burner flame height

The flame height is measured by simply placing a measuring scale next to the flame. Extinction and ignition flame height were not included in the measurement because the flame was flat and rapidly flashing across the burner surface. The flame height measurement is shown in figure 6.8, where it shows that it is a function of the heat release rate of the fuel mixture.

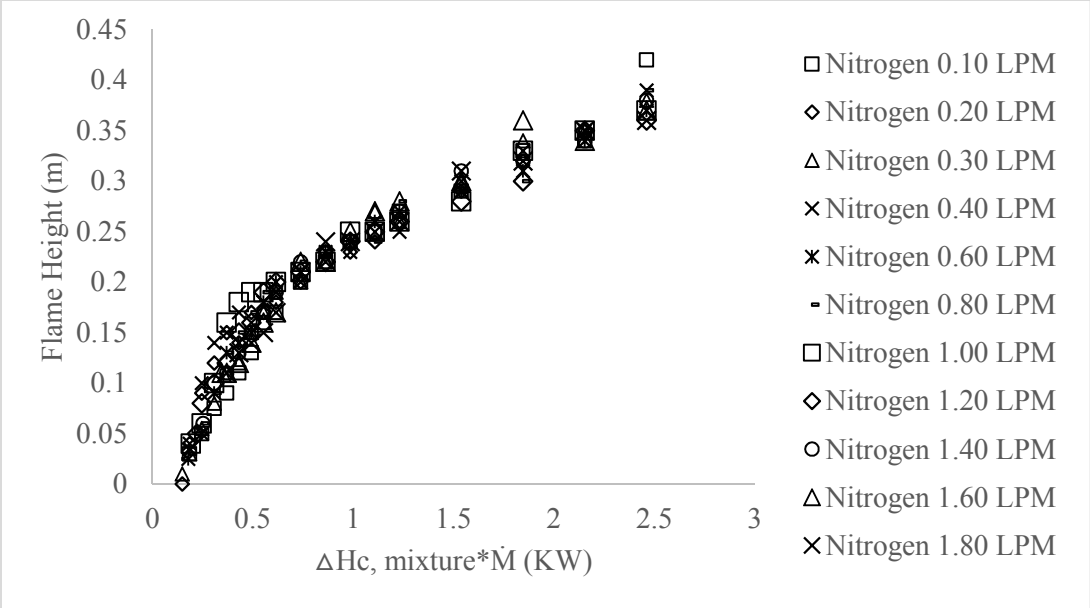

Figure 6.8. Flame height measurement

The flame height measurement can be separated into laminar and turbulent regimes in log-log plot.

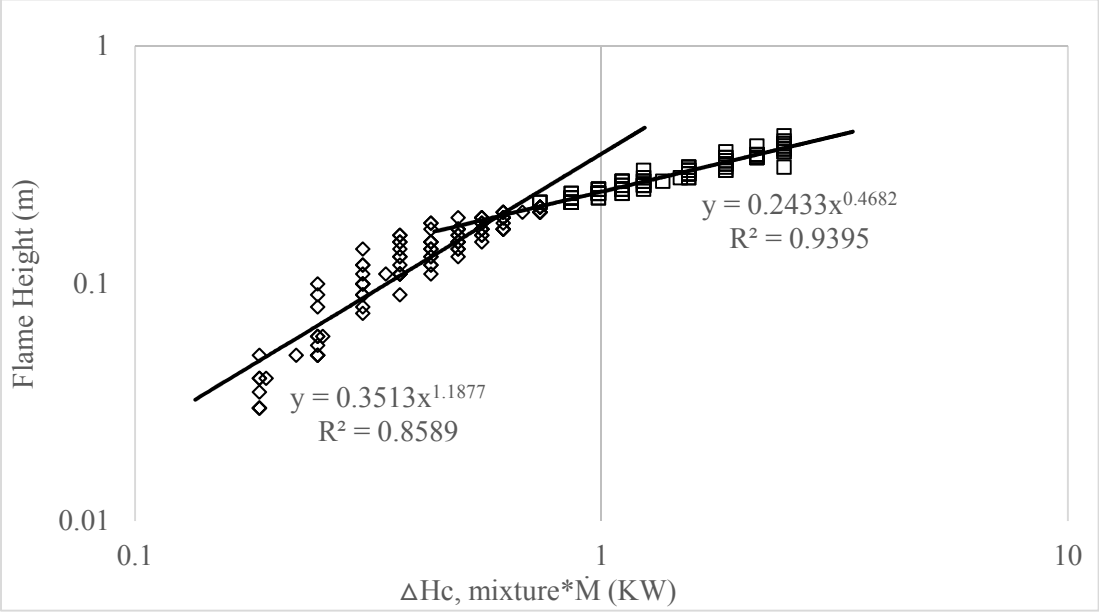

Figure 6.9. Flame height separated into laminar and turbulent regimes

The plot shown in Figure 6.9 agrees with the theory that the slope of the flame height in the laminar region should be 1 and 5/2 for turbulent region. The flame measurement with BRE burner shows a slope of 1.2 for laminar region and 0.47 for turbulent region.

6.3 BRE burner flame radiation fraction

The flame radiant fraction is measured per and is shown in Figure 6.10.

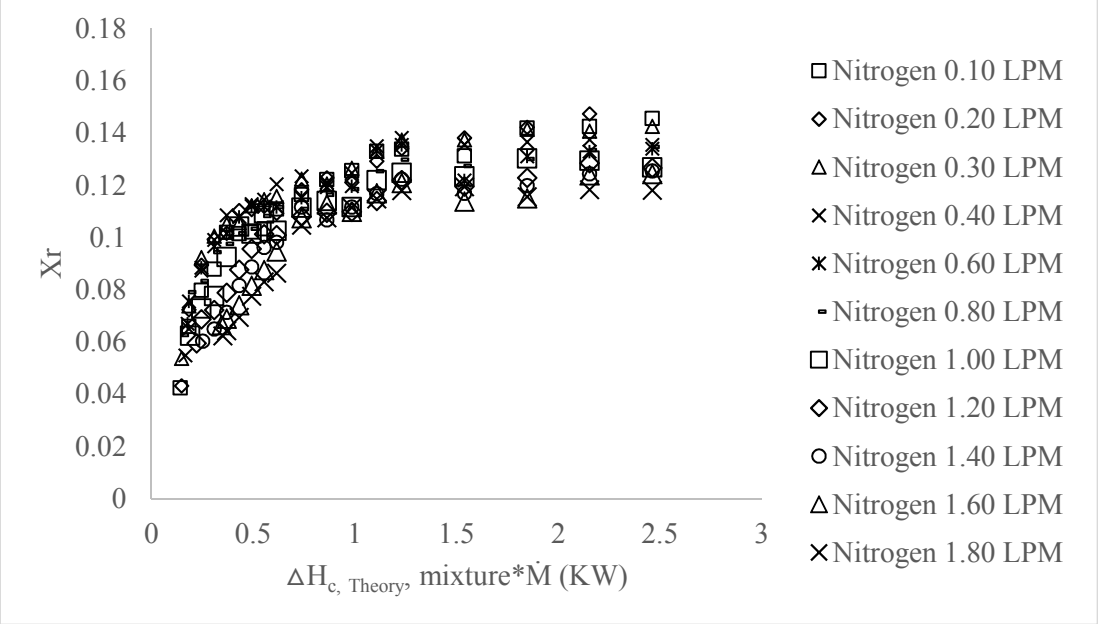

Figure 6.10. Flame radiant fraction measurement

The radiation fraction measurement show that it generally decreases with higher nitrogen dilution rate.

6.3 BRE burner flash, ignition, and extinction point

The mass flux at flash point, ignition, and extinction for condensed fuels is difficult to measure because of the transient nature. The mass flux mass suddenly jump during ignition and extinction. The BRE burner allows clear identification of mass flow of the transient points by gradually changing the fuel flow rate until sustained ignition or

extinction is observed. The experiment was first measured with the brass screen burner with the intention of moving the experiment to copper plate burner. A secondary measurement was taken with the copper plate burner as a comparison and to show that the measurements are not dependent on the burner configuration. The results are shown in Figure 6.11, 6.12, and 6.13.

The flash point and extinction point was measured by gradually increasing the fuel flow rate into the burner. Flash point was established with the first instance of flash across the burner surface. Ignition point is defined as sustained burning of 30 seconds. Extinction point was established by scaling up the fuel flow after ignition, then gradually decreasing the fuel flow rate until flame extinguishes.

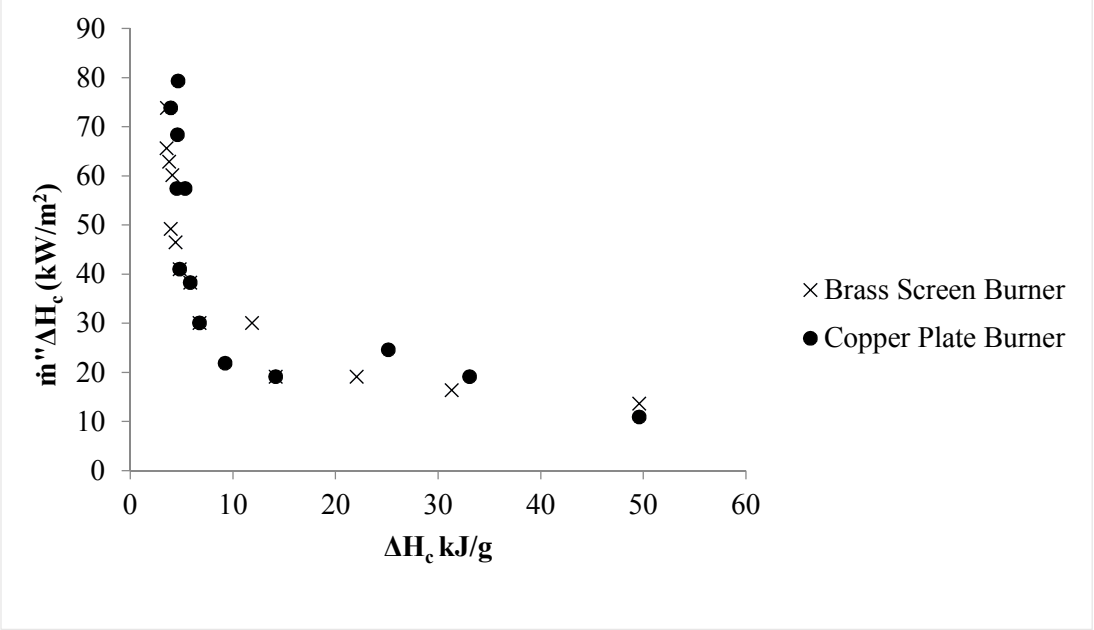

Figure 6.11. Methane flash point measurement with the brass screen and copper plate burner

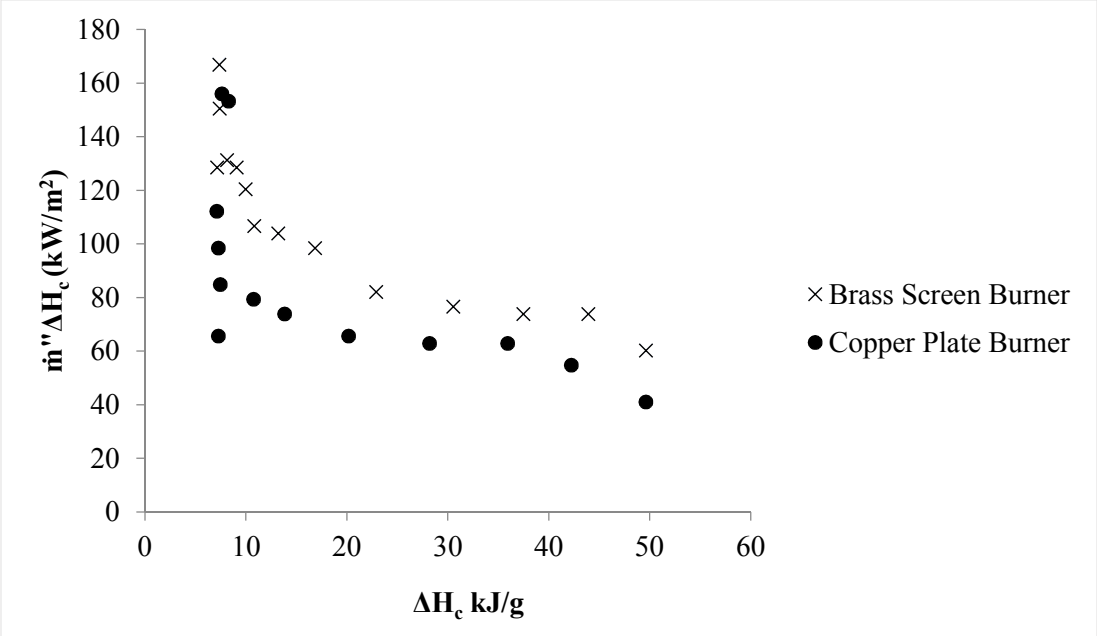

Figure 6.12. Methane ignition point measurement with the brass screen and copper plate burner

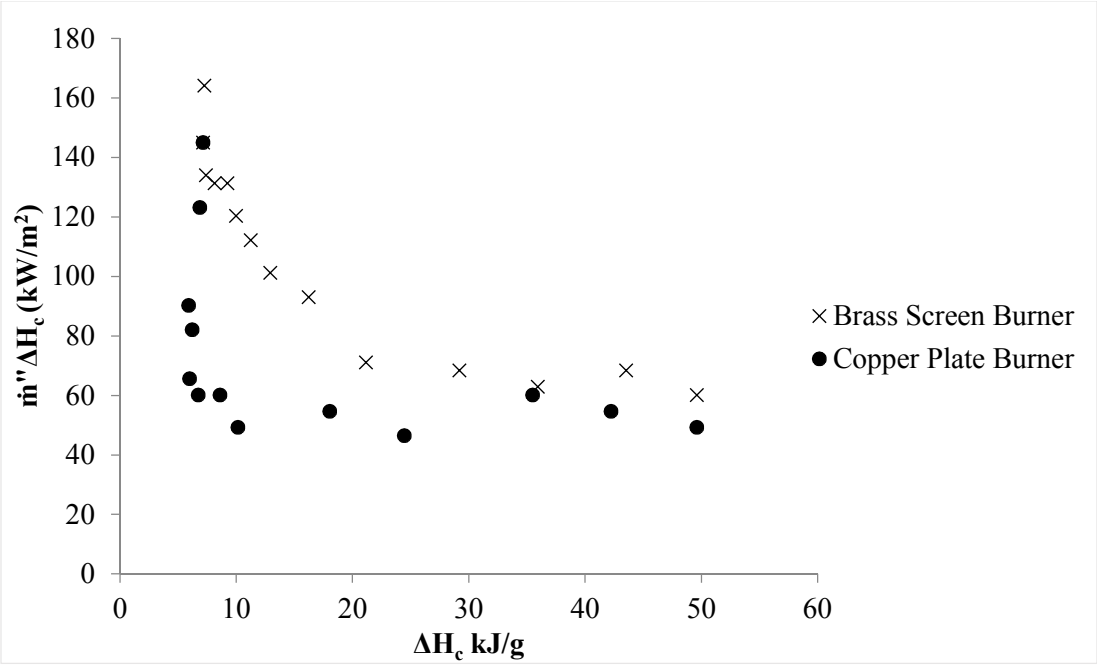

Figure 6.12. Methane extinction point measurement with the brass screen and copper plate burner

The flash, ignition, and extinction point measurement with two burner show good agreement between the measurements. Lyon et al [19], shows extinction data for condensed fuels and examined their dependency with the heat of combustion. The measurements seems to show dependency with the heat of combustion. Further work is being done to study these limits.

Chapter 7: Conclusion

Accurate measurement from a gas-fueled burner has been examined. The calibration and correction process has been developed for heat flux measurements on the burner surface. The local heat flux measurement correction process involves correction via a pure convective burning assumption and takes in to account fuel blockage effects. An optimal paint for the burner and heat flux gauge surface was identified and its absorptivity and emissivity was characterized using two different methods. A radiometer to measure flame radiant fraction also was designed and calibrated. Using these careful calibrations as a basis for accurate measurements, the heat flux distribution across the burner surface has been measured was measured radially at 5 mm intervals from the center.

Experiments with the gas-fueled burner is shown that includes flammability domain, flame height, flame radiant fraction, flash point, ignition point, and extinction point. Further measurement with ethylene and propene with nitrogen gas as diluent will be taken and analyzed with confidence. The accurate data obtained using the outlined procedures are being used better emulate condensed phase burning with the BRE burner. The measurement procedures will be taken to future space flight research with NASA for microgravity research.

Bibliography

1. R. R. Willey; R. W. George; J. G. Ohmart; J. W. Walvoord in: *Total Reflectance Properties Of Certain Black Coatings (From 0.2 To 20.0 Micrometers)*, 1983; 1983; pp 19-26.
2. N. Cholewa; B. Lattimer; S. Case, in: 2013.
3. J. Ballestrín; S. Ulmer; A. Morales; A. Barnes; L. W. Langley; M. Rodríguez, Solar Energy Materials and Solar Cells 80 (3) (2003) 375-381 http://dx.doi.org/10.1016/j.solmat.2003.08.014.
4. I. Dexter Research Center, in: *pdf*, 1m, (Ed.) Dexter Research Center: Michigan, 2000.
5. L. Orloff; J. d. Ris, Symposium (International) on Combustion 13 (1) (1971) 979-992 http://dx.doi.org/10.1016/S0082-0784(71)80098-X.
6. J. S. Kim; J. de Ris; F. William Kroesser, Symposium (International) on Combustion 13 (1) (1971) 949-961 http://dx.doi.org/10.1016/S0082-0784(71)80095-4.
7. J. de Ris; L. Orloff, Symposium (International) on Combustion 15 (1) (1975) 175-182 http://dx.doi.org/10.1016/S0082-0784(75)80295-5.
8. L. Brahmi; T. Vietoris; S. Rouvreau; P. Joulain; L. David; J. L. Torero, AIAA journal 43 (8) (2005) 1725-1733
9. Y. Zhang; M. J. Bustamante; M. J. Gollner; P. B. Sunderland; J. G. Quintiere, Journal of Fire Sciences 32 (1) (2014) 52-71
10. B. Michael. Experimental Investigation of Liquid and Gas Fueled Flames Towards the Development of a Burning Rate Emulator (BRE) for Microgravity Applications. University of Maryland, College Park, 2012.
11. J. G. Quintiere, Fundamentals of fire phenomena, John Wiley, Chichester, 2006, p.^pp.
12. J. P. Holman, Heat transfer, McGraw-Hill, New York, 1976, p.^pp.
13. in: Medtherm Corporation: Huntsville, 2002.
14. W. M. Pitts; A. V. Murthy; J. L. de Ris; J.-R. Filtz; K. Nygård; D. Smith; I. Wetterlund, Fire Safety Journal 41 (6) (2006) 459-475 http://dx.doi.org/10.1016/j.firesaf.2006.04.004.
15. R. H. J. R. Siegel, Thermal radiation heat transfer, Hemisphere Pub. Corp., Washington, 1981, p.^pp.
16. M. L. d. Zukunft, in: Mankiewicz Gebr. & Co.: Hamburg, p 2.
17. K. McGrattan; S. Hostikka; R. McDermott; J. Floyd; C. Weinschenk; K. Overholt, in: 6 ed.; National Institute of Standards and Technology: 2014; Vol. 1019, p 268.
18. K. B. McGrattan; H. R. Baum; A. Hamins, National Institute of Standards & Technology, US Department of Commerce, Washington, DC (2000)
19. R. E. Lyon; J. G. Quintiere, Combustion and Flame 151 (4) (2007) 551-559 http://dx.doi.org/10.1016/j.combustflame.2007.07.020.